Single-Cell Multiomic Analysis of Circadian Rhythmicity in Mouse Liver

Chun Yip Tong[1], Changhao Li[2], Clémence Hurni[3], Audrey Jacq[1], Xinyu Y Nie[1], Chanté R. Guy[1], Ju Hyun Suh[2], Raymond K.W. Wong[2], Christine Merlin[1,4], Felix Naef[3], Jerome S Menet[1,4,*], Yuchao Jiang[1,2,4,5,6,*]

1. Department of Biology, College of Arts and Sciences, Texas A&M University, College Station, TX, USA.
2. Department of Statistics, College of Arts and Sciences, Texas A&M University, College Station, TX, USA.
3. The Institute of Bioengineering (IBI), School of Life Sciences, Ecole Polytechnique Fédérale de Lausanne (EPFL), Lausanne, Switzerland.
4. Center for Biological Clocks Research, Texas A&M University, College Station, TX, USA.
5. Department of Biomedical Engineering, College of Engineering, Texas A&M University, College Station, TX, USA.
6. Center for Statistical Bioinformatics, Texas A&M University, College Station, TX, USA.

*. To whom correspondence should be addressed: menet@bio.tamu.edu, yuchaojiang@tamu.edu.

ABSTRACT

From bacteria to humans, most organisms showcase inherent 24-hour circadian rhythms, best exemplified by the sleep-wake cycle. These rhythms are remarkably widespread, governing hormonal, metabolic, physiological, and behavioral oscillations, and are driven by molecular clocks that orchestrate the rhythmic expression of thousands of genes throughout the body. Here, we generate single-cell RNA and ATAC multiomic data to simultaneously characterize gene expression and chromatin accessibility of ~33,000 mouse liver cells across the 24-hour day. Our study yields several key insights, including: (i) detecting circadian rhythmicity in both discretized liver cell types and transient sub-lobule cell states, capturing space-time RNA and ATAC profiles in a cell-type- and cell-state-specific manner; (ii) delving beyond mean cyclic patterns to characterize distributions, accounting for gene expression stochasticity due to transcriptional bursting; (iii) interrogating multimodal circadian rhythmicity, encompassing RNAs, DNA regulatory elements, and transcription factors (TFs), while examining priming and lagging effects across modalities; and (iv) inferring spatiotemporal gene regulatory networks involving target genes, TFs, and cis-regulatory elements that controls circadian rhythmicity and liver physiology. Our findings apply to existing single-cell data of mouse and *Drosophila* brains and are further validated by time-series single molecule fluorescence in situ hybridization, as well as vast amounts of existing and orthogonal high-throughput data from chromatin immunoprecipitation followed by sequencing, capture Hi-C, and TF knockout experiments. Altogether, our study constructs a comprehensive map of the time-series transcriptomic and epigenomic landscapes that elucidate the function and mechanism of the liver peripheral clocks.

INTRODUCTION

From bacteria to humans, most organisms exhibit inherent 24-hour circadian rhythms [1]. Best exemplified by the sleep-wake cycle, these rhythms are remarkably widespread, governing hormonal, metabolic, physiological, and behavioral oscillations and enabling biological functions to perform optimally at the most appropriate time of the day [2-4]. Circadian rhythms are driven by an autonomous and intrinsic timekeeping system known as the circadian clock [5,6], which is genetically orchestrated by a set of core clock activator and repressor transcription factors (TFs) interlocked in three transcription-translation feedback loops [7]. These TFs bind to E-boxes [8], ROREs [9], or D-boxes [10] in the promoters and enhancers of specific target genes to generate cycles of transcription with various phases. Disruption of circadian rhythm has been associated with sleep disorders [11], major depression disorder [12], cancer [13], metabolic syndrome [14], Alzheimer's disease [15], and aging [16], highlighting the significant role of molecular circadian clocks in physiological processes and disease outcomes.

Recent advances in high-throughput omics technologies provide appealing platforms for identifying circadian genes [17] and uncovering the mechanisms that underlie their rhythmic expression [18] on the genome-wide scale. In a typical high-throughput experiment, tissues are collected at six to eight different zeitgeber time (ZT) or circadian time (CT) points, followed by omics profiling such as RNA sequencing (RNA-seq) to generate time-series expression profiles. While significant efforts have yielded notable successes – see, for example, existing benchmark studies [19-21] and omics databases [22-24], bulk-tissue sequencing homogenizes potentially different cell types and cell states, where thousands to millions of cells are pooled with an averaged readout, masking the intricate cellular heterogeneity. Single-cell sequencing, on the other hand, circumvents the averaging artifacts by enabling cellular-level measurements with a much finer resolution.

Four single-cell RNA-seq (scRNA-seq) studies have generated time-series transcriptomic profiles of cells from mouse suprachiasmatic nucleus (SCN) [25], mouse clock neurons [26], mouse livers [27], and *Drosophila* brains [28] at different ZT or CT time points. The pioneering studies by Wen et al. [25] and Ma et al. [26] focused on identifying rhythmic genes within specific cell types or subtypes of the mouse brain. Dopp et al. [28] recently investigated cell-type-specific rhythmicity not only across four ZT time points but also under different sleep or wakefulness states of the *Drosophila* brain cells. Expanding beyond discretized cell types and clusters, Droin et al. [27] first adopted scRNA-seq to infer circadian rhythmicity in transient cell states of liver hepatocytes. The mouse liver consists of diverse cell types, including hepatocytes, Kupffer cells, fibroblasts, endothelial cells, T cells, and B cells [29]. Furthermore, the hepatocytes exhibit a distinct spatial trajectory due to the liver's anatomical compartmentalization into lobular and sub-lobular zonation [27], where a gradient of oxygen and nutrient concentrations along the periportal-pericentral axis drives the metabolic and physiological functions of

52 hepatocytes [30]. This pronounced cell-type and cell-state specificity enables the interrogation of spatiotemporal
53 gene expression and provides deeper insights into gene regulation across both space and time.
54
55 Single-cell data is inherently noisy, and treating cells as independent samples inflates the effective sample size
56 and thus the type I error. To address this, existing studies pooled similar cells through averaging as a common
57 approach. However, this common approach largely forfeits the purpose of single-cell sequencing, which
58 characterizes distributions of gene expression, going beyond the mean measurements. The stochastic nature of
59 gene expression, driven by the pervasive phenomenon of transcriptional bursting, has been previously explored
60 in scRNA-seq data [31,32]. Yet, relating transcriptional bursting to circadian rhythm on the genome-wide scale using
61 time-series single-cell data remains largely underexplored, except for a few studies that adopted single molecule
62 fluorescence in situ hybridization (smFISH) on a limited number of genes [33,34].
63
64 Beyond transcriptomic studies [35], bulk-tissue circadian investigations have successfully examined epigenome [36,37],
65 metabolome [38], acetylome [39], and proteome [40], while existing single-cell circadian studies to date [25-28] have been
66 limited exclusively to the transcriptome. To our best knowledge, no time-series single-cell assay for transposase-
67 accessible chromatin (ATAC) with sequencing data currently exist that temporally profile genome-wide
68 chromatin accessibility, resulting in several missed opportunities. First, the multimodal rhythmicity of chromatin
69 accessibility across gene bodies, regulatory regions such as promoters and enhancers, and TF-binding motifs
70 remains unexplored. Second, genome-wide mapping of cell-type- and cell-state-specific regulatory regions that
71 are linked to rhythmic gene expressions has yet to be systematically conducted. Third, while inferring gene
72 regulatory logic [41] involving a target gene, a cis-regulatory element (CRE), and a TF regulator by single-cell
73 omics data has seen rapid methodological development, the application of these approaches to decipher cell-type-
74 and cell-state-specific regulatory networks of circadian gene expression has remained untapped.
75
76 In this study, we generate the first single-cell RNA and ATAC multiomic data at six different circadian time
77 points across the 24-hour cycle, simultaneously measuring RNA expression of ~32,000 genes and DNA
78 accessibility of ~150,000 peaks in ~34,000 mouse liver cells. We detected circadian rhythmicity in both
79 discretized liver cell types and transient sub-lobule cell states, revealing spatiotemporal RNA and ATAC profiles
80 in a cell-type- and cell-state-specific manner. Moving beyond mean measurements, we characterized gene
81 expression distributions and demonstrated that the fraction of bursting cells closely recapitulate the rhythmicity
82 seen in averaged expression, as traditionally measured. We explored multimodal circadian rhythmicity and
83 examined priming and lagging effects across modalities. For gene regulation, we linked CREs to target genes and
84 further inferred gene regulatory logic involving target gene, TFs, and CREs for circadian control. We validated
85 our findings using time-series smFISH, as well as the vast amounts of existing and orthogonal high-throughput

86 data from chromatin immunoprecipitation followed by sequencing (ChIP-seq), capture Hi-C, and TF knockout
87 experiments. Furthermore, we reproduced key results in existing scRNA-seq data of mouse and *Drosophila* brains.
88 Altogether, our research constructs a comprehensive map of the transcriptomic and epigenomic landscapes that
89 underpin the function and mechanism of the liver peripheral clocks.
90

91 **RESULTS**

92 **Single-nucleus RNA and ATAC multiomic profiling of mouse liver across circadian time points**

93 Using 10x Genomics' Single Cell Multiome ATAC + Gene Expression solution, we jointly charaterized gene
94 expression and chromatin accessibility of more than 33,000 mouse liver nuclei, collected at six Zeitgeber time
95 (ZT) points over a 24-hour period under a light-dark experimental design (**Fig. 1A**). Detailed protocols for tissue
96 collection, nuclei isolation, library preparation, and sequencing can be found in the Methods section. Our overall
97 analysis framework is outlined in **Fig. S1**. We began with doublet removal and quality control (QC) using both
98 the RNA and ATAC modalities, resulting in a genome-wide profiling of 16,368 gene expressions and 149,302
99 peak accessibilities (**Fig. S2**). It is worth noting that while the multiome protocol primarily detects nuclear
100 transcripts, reflecting "nuclear RNA expression," we use "expression" to lighten the terminology. Using the
101 ATAC fragments, we further derived gene-specific ATAC activity scores [42], which quantify the accessibility of
102 gene bodies and promoters, as well as TF-specific motif deviation scores [43], which assess the overall accessibility
103 of corresponding TF-binding motifs (**Fig. 1A**).
104

105 Within each of the four modalities (i.e., RNA expression, ATAC accessibility, gene activity, and motif deviation
106 score), we first performed within-modality data normalization, batch-effect correction across circadian time
107 points, and post-correction dimension reduction (**Fig. S3**). This was followed by between-modality data
108 integration via multiple canonical correlation analysis (multiCCA) to borrow information across different
109 modalities [44] (**Fig. 1B**). Cell-type labels were transferred from the Liver Cell Atlas (LCA) [29] by integrating the
110 RNA domains (**Fig. S4**). This analytical framework effectively identified and distinctly clustered seven major
111 liver cell types: hepatocytes, endothelial cells, fibroblasts, Kupffer cells, cholangiocytes, B cells, and T cells (**Fig.**
112 **1B**). Notably, as previously reported by the LCA [29], isolation of liver nuclei leads to enrichment of hepatocytes
113 while depleting endothelial cells – a trend we also observed in our data.
114

115 As a sanity check, we examined previously reported cell-type-specific marker genes and confirmed that they were
116 enriched within their respective cell types for both the RNA and ATAC modalities (**Fig. 1C**). On the genome-
117 wide scale, cell-type-specific gene expressions from our study closely recapitulated those previously identified
118 by the LCA [29], with near-perfect correlation coefficients (**Fig. S5**). Additionally, the ATAC peaks that we detected
119 overlapped with over 90% of the existing bulk-tissue DNase I hypersensitive sites (DHSs) of the mouse liver [45].

With enhanced cellular resolution, we also detected a signficant number of novel peaks that were validated by histone modifications, serving as candidate CREs (**Fig. S6**).

For circadian rhythm detection, we first sought to reproduce the cyclic patterns previously reported in mouse liver at the bulk-tissue level. To do this, we randomly grouped all cells into two pseudo-bulk samples, analagous to the two replicates in traditional bulk-tissue sequencing. The top 2,000 circadian genes previously identified in mouse liver [46] were visualized as heatmaps for both RNA expression and ATAC activity, revealing a clear genome-wide rhythmic pattern in both modalities (**Fig. 1D**). This provides strong empirical support that our generated data can detect genome-wide rhythmicity in chromatin accessibility associated with rhythmic RNA expression. We then trained a deep neural network (DNN) that takes as input gene expression measurements to predict the ZT time point. In the held-out single-cell validation set, the DNN achieved an astounding 99.8% accuracy; in a test set of 1,096 time-series GRO-seq [47], Nascent-seq [48], and RNA-seq [48] samples from 57 public repositories [35], the model achieved a strong correlation between the predictions and the ground truths ($r = 0.84$) (**Fig. S7**). This not only provides a versatile tool to make a prediction of circadian time [49] but also highlights the high quality of our time-series transcriptomic and epigenomic profiles of mouse liver.

Cell-type-specific rhythmic RNA expression and ATAC accessibility predominantly in hepatocytes

Using the normalized, batch-corrected, and integrated multi-modal data along with the transferred cell-type labels, we next investigated cell-type-specific rhythmicity across different modalities, focusing on four major cell types – hepatocytes, endothelial cells, fibroblasts, and Kupffer cells (**Fig. 2A**). To ensure an unbiased comparison with an equal testing power across cell types, we downsampled cells from different cell types to retain the same cell count at each timepoint. Additionally, and more importantly, to strike a balance between type I error control and statistical power and to enhance signal-to-noise ratio in the highly sparse and noisy single-cell data, we pooled similar cells together and constructed metacells at each ZT time point. The number of metacells was determined using gold-standard rhythmic and arrhythmic genes as positive and negative controls [50] (**Fig. S8**; see the Method section for more details). Given the time-series omic profiles of the reconstructed metacells, we tested for significant circadian rhythmicity by integrating results from both JTK cycle [51,52] and harmonic regression [53] via a combination testing framework [54], followed by multiple testing correction (**Fig. S9**).

Genome-wide cell-type-specific testing results of circadian rhythmicity are presented in **Table S1**. Examining 13 core clock and clock reference genes (*Arntl*, *Bhlhe40*, *Bhlhe41*, *Clock*, *Npas2*, *Dbp*, *Nfil3*, *Nr1d1*, *Rorc*, *Cry1*, *Ciart*, *Per1*, and *Per2*), we found that nearly all exhibited significant cyclic patterns in hepatocytes for both RNA expression and ATAC activity (**Fig. 2A**). However, in the other cell types (i.e., endothelial cells, fibroblasts, and Kupffer cells), only a subset of the clock genes displayed significant rhythmicity (**Fig. 2A**, **Fig. S10**). For example,

154 *Clock* and *Npas2*, key regulators of the clock through their heterodimeric interactions with *Arntl*, were only
155 significantly rhythmic in hepatocytes and fibroblasts. Consistent with this, a previous study using total RNA-seq
156 confirmed that *Clock* and *Npas2* are not rhythmic in isolated Kupffer cells [55]. A similar pattern emerged at the
157 genome-wide scale, with hepatocytes harvesting the highest number of uniquely identified rhythmic genes among
158 all cell types (**Fig. 2B**). Phase set enrichment analysis (PSEA) [56] of cell-type-specific rhythmic genes further
159 revealed distinct phase-clustered functional enrichments (**Fig. 2C**, **Fig. S11**). Altogether, our findings reveal
160 significant cell-type-specific rhythmic patterns, aligning with previous scRNA-seq studies of circadian rhythms
161 [25,26]. In the mouse liver, we demonstrate that hepatocytes – known to play a crucial role in cells' metabolic
162 functions such as glucose metabolism, lipid metabolism, and detoxification [57] – exhibit the most pronounced
163 rhythmic patterns across various modalities of the peripheral clock.
164
165 Moving beyond RNA expression to compare across modalities, we identified 3,638 significantly rhythmic genes
166 in RNA expression and 2,307 in ATAC activity, with 4,431 genes exhibiting rhythmicity in both, using the entire
167 set of hepatocytes (**Fig. 2D**). For genes that are rhythmic for both modalities, their phases of RNA expression and
168 ATAC activity are highly correlated ($r = 0.81$; **Fig. 2E**). We further tested for significant phase shifts between
169 the two modalities using CircaCompare [58]. Clock genes such as *Arntl* and *Npas2* exhibit synchronized rhythmicity,
170 while the ATAC activity of *Per1*, *Clock*, and *Nr1d1* harbors an earlier phase than RNA expression, suggesting a
171 temporal relationship between chromatin state and transcription (**Fig. 2F**). On a genome-wide scale, genes with
172 significantly smaller ATAC phases (i.e., those where ATAC rhythmicity primes RNA rhythmicity) are longer
173 and exhibit higher relative amplitude (rAMP) (**Fig. 2G**), potentially due to their greater need for chromatin
174 priming. Notably, for genes with smaller RNA phases, while their precise regulatory mechanism requires further
175 investigation beyond the scope of this paper, a recent study [59] suggested that chromatin remodeling occurs four
176 hours after transcription – the translational process facilitates chromatin remodeling [59] and meanwhile transcribed
177 RNAs form R-loop structures with CREs to promote recruitment of epigenetic modifiers [60].
178
179 Next, we analyzed 746 TFs with annotated binding motifs from the JASPAR database [61]; we found that 32% of
180 these TFs exhibited significant rhythmicity in gene expression, ATAC activity, and motif scores (**Fig. S12A**),
181 with genome-wide results shown in **Table S2**. Notably, differences between TF gene expressions and TF motif
182 scores likely result from their distinct measures of transcription and DNA binding. For TF-binding motifs,
183 deviation scores of E-box motifs (ARNTL, CLOCK, BHLHE40, and BHLHE41), D-box motifs (DBP and
184 NFIL3), and RORE motifs (NR1D1 and RORC) display distinct phases, demonstrating their collective function
185 to regulate rhythmic gene expression around the clock (**Fig. S12B**). Importantly, TF-specific rhythms were also
186 more pronounced in hepatocytes than in the other cell types – some exhibited unique circadian patterns, while

187 others showed heightened relative amplitudes (**Fig. S12B**) – aligning with our previous observations based on the
188 gene-level testing results.
189
190 In addition to aggregating ATAC fragments into either gene activity or motif deviation scores, we identified
191 25,582 ATAC peaks (17.1% of ~150K peaks) with significant rhythmic accessibility. This contrasts with a
192 previous bulk-tissue study, which identified 8% of ~65K DHSs as cyclic [62], highlighting the enhanced resolution
193 and increased testing power. We further carried out a phase-specific motif enrichment analysis using the
194 significantly cyclic peaks (**Fig. 2H**). We discovered enrichment of E-box motifs from ZT06 to ZT09, D-box
195 motifs from ZT09 to ZT15, as well as RORE and RevDR2 motifs from ZT18 to ZT24, consistent with a recent
196 report [47]. Interestingly, we also found that the binding motifs for KLF15 and KLF10 were highly enriched between
197 ZT00 and ZT06. The Krüppel-like family of transcription factors (KLFs) are known to play essential roles in liver
198 physiology and metabolism [63]; previous research has shown that *Klf15* and *Klf10* expression is strongly induced
199 in the liver during fasting, aligning with the observed enriched timeframe [64]. Additionally, the binding motifs of
200 Retinoid X Receptor Alpha (RXRA) and Peroxisome Proliferator-Activated Receptor Delta (PPARD) were
201 highly enriched between ZT15 and ZT18; both genes play critical roles in metabolic processes linked to the
202 feeding cycle, functioning as a heterodimer to regulate lipid metabolic pathways [65].
203
204 **Beyond mean measurements: rhythmic nuclear gene expression driven by rhythmic bursting fraction**
205 Single-cell sequencing circumvents the averaging artifacts associated with traditional bulk-tissue sequencing, thus
206 enabling characterization of not only mean measurements but also distributions. To date, several scRNA-seq
207 studies [31,32] have demonstrated that cellular gene expression is highly stochastic, resulting from the pervasive
208 phenomenon of transcriptional bursting, where cells switch between "ON" and "OFF" transcriptional states.
209 While pioneering studies have adopted time-series smFISH to study circadian rhythmicity in relation to promoter-
210 enhancer looping and transcriptional bursting [27,34,66], they focused on a limited set of clock genes (e.g., *Arntl*,
211 *Nr1d1*, and *Cry1*, as shown in **Fig. S13**), leaving behind a missed opportunity for comprehensive genome-wide
212 profiling.
213
214 To systematically investigate the relationship between transcriptional bursting and circadian rhythm, we tested
215 two different underlying models that can both result in cyclic gene expressions: rhythms in average expression
216 across the majority of cells (Model 1) and rhythms in the fraction of bursting cells (Model 2) (**Fig. 3A**). For model
217 1, we calculated the average expression across all cells comprising the metacell, while for model 2, we computed
218 the fraction of cells with non-zero expression. Both the average expression and the bursting-cell fraction measured
219 at the metacell level at different timepoints were used as input to detect circadian rhythmicity. Note that these two
220 measures differ, as single-cell gene expression measurements from unique molecular identifier (UMI)-based

221 protocols have been shown to follow a Poisson distribution [67]. Without loss of generality, we focused on
222 hepatocytes and later extended the testing framework to other cell types, tissues, and species. Interestingly, in
223 hepatocytes, all core clock and clock reference genes – including *Arntl*, *Per1*, *Per2*, *Npas2*, *Dbp*, *Cry1*, *Clock*,
224 *Nr1d1*, and *Rorc* – exhibited significant rhythmicity for both mean RNA expression and the proportion of cells
225 with non-zero expression (i.e., the fraction of bursting cells), with nearly identical cosinor curves (**Fig. 3B**). Our
226 results strongly suggest that the mean of binarized expression (i.e., the fraction of cells with non-zero expression)
227 closely mirrors the mean of the absolute integer-valued expression in the circadian context. Biologically, this
228 indicates that the fraction of cells actively transcribing RNAs varies between the peak and trough, regardless of
229 the burst magnitude or the quantity of RNAs produced. This observation, combined with the widespread
230 monoallelic expression observed at the single-cell level [68,69] due to transcriptional bursting, overwhelmingly
231 supports model 2 over model 1.
232
233 Extending the investigation to the genome-wide scale, approximately 54% of rhythmic genes showed significant
234 rhythmicity in both mean expression and bursting-cell fraction (**Fig. 3C**). Of the 2,336 genes with rhythmic mean
235 expression and the 1,155 genes with rhythmic bursting-cell fraction, the former group shows significantly less
236 "burstiness" and higher expression levels (**Fig. 3D**). The bursting kinetics of constitutively expressed genes (e.g.,
237 housekeeping genes) become statistically intractable due to identifiability issues, as previously reported [31,70].
238 Therefore, due to the lack of burstiness, accurately inferring their bursting parameters when fitting the Poisson-
239 Beta hierarchical model is neither possible nor necessary. When comparing rhythmic genes identified based on
240 the mean expression, the proportion of cells with non-zero expression (a surrogate for burst frequency), and the
241 mean of non-zero expression (a surrogate for burst size), we found significant overlap between the first two groups
242 of genes (**Fig. S14A**). Additionally, Gini index and coefficient of variation – both measuring variability – were
243 highly correlated with mean expression and the fraction of bursting cells (**Fig. S14B**), indicating that biological
244 variation also exhibits significant rhythmic patterns.
245
246 For reproducibility, both gene-specific and genome-wide results apply to existing time-series scRNA-seq data of
247 mouse SCN [25] (**Fig. S15**) and *Drosophila* neuron [26] (**Fig. S16**). Across all datasets, adjusted p-values, phases, and
248 amplitudes showed strong correlations between testing of cyclic mean expression and cyclic bursting-cell fraction
249 (**Fig. 3E**). For validation, we utilized previously published smFISH data with both mean mRNA concentration
250 and proportion of cells with detectable transcripts in the nuclei for *Arntl* and *Per1* [27] (see Method for detail).
251 Consistent with our single-nucleus sequencing results, the rhythmic pattern of the bursting-cell fraction closely
252 mirrors that of the mean measurement – the nuclear RNA concentration calculated across cell nuclei on a log
253 scale for variance stabilization (**Fig. 3F**). Collectively, our results, overwhelmingly supported by empirical
254 evidence from extensive orthogonal and independent omics resources, suggest that circadian rhythmicity is

255 predominantly driven by burst frequency rather than burst size. We further relate this discovery and conclusion
256 to other biological contexts in the Discussion section.
257
258 **Spatiotemporal gene expression and CRE accessibility in hepatocytes across the liver lobules**
259 So far, our analyses have focused on discretized cell types, while the mammalian liver also comprises transient
260 cell states due to its hexagon-shaped lobules, with central vein (CV) at the center and portal triad at the corners
261 (**Fig. 4A**). The portal triad consists of a portal node (PN), portal artery, and bile duct. Blood flows from the PN
262 towards the CV through sinusoids, creating a directional gradient of oxygen, nutrients, and hormones [71,72]. To
263 infer spatial zonation [27,30] of our sequenced cells along the lobule axis, we performed trajectory reconstruction
264 using Slingshot [73] and inferred pseudotime, a fractional measure capturing cells' spatial positioning along the PN-
265 to-CV axis (**Fig. 4B**). As expected, previously reported [30] gene markers *Cyp2f2* and *Cyp2e1* were predominantly
266 expressed and accessible in periportal and pericentral hepatocytes near the PN and CV, respectively (**Fig. 4C**).
267
268 Given the circadian time points and the inferred spatial zonation of the cells, we devised a statistical framework
269 to test whether each gene's RNA expression and ATAC activity exhibit spatial, circadian, or combined spatial
270 and circadian patterns (**Fig. 4D).** See Method for details and **Fig. S17** for testing results of representative genes.
271 Our results revealed that *Arntl* – a core clock gene – was circadian but not spatial, ensuring a robust circadian
272 control across the hepatic zonation [27] (**Fig. 4E**). The other clock reference genes all exhibited significant cyclic
273 patterns, although some were also spatially variable, especially when jointly tested across both time and location
274 (**Fig. S18**). In contrast, *Glul*, which was previously shown to be spatially enriched at the CV [71], was spatially
275 variable but not circadian (**Fig. 4E**). At the genome-wide level, we identified transient genes with spatially
276 variable RNA expression and/or ATAC activity enriched near the PN and CV, followed by KEGG pathway
277 enrichment analysis (**Fig. S19**). For spatiotemporal expression, we identified 2,343 genes across the genome that
278 were both spatially variable and rhythmic over time. Importantly, the joint testing framework across both spatial
279 location and circadian timepoint identified spatial and circadian genes that were otherwise masked when testing
280 by location or timepoint alone, highlighting the utility of the spatiotemporal approach (**Fig. S17**). **Fig. 4F**
281 highlights three representative spatial and circadian genes – *Acly*, *Pck1*, and *Elovl3* – that exhibit significant
282 space-time variation. Their spatiotemporal patterns were further validated by time-series smFISH of mouse liver
283 [27]. Additionally, we identified a novel spatial and circadian gene, *Agxt*, which encodes alanine-glyoxylate
284 aminotransferase, a key enzyme for glyoxylate metabolism in mouse liver. Newly generated smFISH data of *Agxt*
285 confirmed its expression pattern (**Fig. 4G**). Notably, beyond RNA expression, ATAC activity of genes also
286 demonstrated similar spatiotemporal patterns (**Fig. S20**).
287

288 The liver's peripheral clock is governed by intricate gene regulatory networks. While previous studies have
289 demonstrated the circadian and transient expression of genes along the liver lobule [27], the underlying gene
290 regulatory mechanisms remain largely unexplored. Utilizing the paired ATAC modality, we linked open-
291 chromatin regions (i.e., CREs) to target gene expressions by testing for significant association between chromatin
292 accessibility and gene expression (see the Method for details). Importantly, this association was tested across both
293 spatial and temporal dimensions, allowing us to identity spatial, circadian, and spatial & circadian CREs. Three
294 representative CRE-gene pairs were visualized in **Fig. 4H**. Specifically, *Arntl*, a core clock gene, exhibited
295 significant temporal correlations with circadian CREs. Motif enrichment analysis using the linked CREs returned
296 significant enrichment of the RORA motif, consistent with the role of the ROR family as key regulators of *Arntl*
297 [74] (**Fig. 4H**). Additional circadian CREs were also identified for other clock genes, including *Clock*, *Cry1*, *Dbp*,
298 *Nr1d1*, and *Rorc* (**Fig. S21**). In contrast, *Glul*, the previously identified spatially variable gene, was significantly
299 associated with spatial CREs enriched for the TCF7L2 binding motifs [75] (**Fig. 4H**). Interestingly, *Pck1*, a circadian
300 and transient gene, displayed spatial, temporal, and spatiotemporal correlations with CREs enriched for the
301 binding motif of PPARG and RXRA; these TFs form a heterodimer to regulate the expression of *Pck1*, which is
302 essential for the maintenance of lipid metabolism [76] (**Fig. 4H**).
303
304 Genome-wide, we identified over 30,000 circadian CREs, 10,000 spatial CREs, and 750 spatial & circadian CREs
305 (**Fig. 4I**). Detailed linkage results are presented in **Table S3**, with top significantly enriched motifs from the linked
306 CREs displayed in **Fig. S22**. For validation, we utilized existing ChIP-seq data for the enhancer histone markers
307 H3K27ac and H3K4me1 [77] enriched at active and primed enhancers; both markers showed significant enrichment
308 at spatial, circadian, and spatial & circadian CREs, compared to random genomic regions (**Fig. 4J**). By leveraging
309 paired RNA and ATAC modalities characterized at the single-cell level, we were able to identify different types
310 of enhancers (i.e., CREs) linked to the same target genes across circadian timepoints and lobular zonation, with
311 corresponding motif enrichments for clock and liver-specific metabolic TFs (**Fig. 4K**). These genome-wide
312 results provide strong empirical support for the classic model of an integrative regulatory mechanism involving
313 multiple CREs with TF-binding motifs [78,79].
314
315 **Three-way relationships between CREs, TFs, and target genes for circadian regulation**
316 Understanding how TFs interact with CREs to regulate target gene expression is essential for elucidating the
317 molecular mechanisms for circadian control. Traditional approaches adopted ChIP-seq to detect TF binding at
318 potential CREs [80]. Target genes are, however, not directly inferred and are typically assigned based on their
319 proximity to the CREs, often limiting the focus of CREs primarily to the genes' promoter regions. While the
320 previous section linked more distant CREs to target genes, CRE-gene linkage analysis does not provide direct
321 information on TF binding either – motif enrichment analysis using these linked CREs is a two-step approach

322 that further suffers from reduced resolution of TF binding. In this regard, the single-cell multiomic design enables
323 time-series characterizations of CRE accessibility, TF binding, and target gene expression, all measured
324 simultaneously in the same cells, offering unprecedented opportunities to directly infer regulatory relationships
325 among these factors.
326
327 Leveraging the recently developed TRIPOD [41] framework – a computational approach for detecting three-way
328 regulatory relationships among TFs, CREs, and target genes using single-cell multiomics data – we next sought
329 to detect regulatory "trios," where a TF binds to a CRE to regulate target gene expression (**Fig. 5A**). Specifically,
330 TRIPOD takes as input the motif score of a TF (replacing the default TF expression to more accurately capture
331 binding activity and regulatory potential), the accessibility of a candidate CRE, and the expression of a gene to
332 infer the CRE-TF-gene relationship, with genome-wide results shown in **Table S4**. **Fig. 5B** outlines three
333 significant trios that are in line with the transcriptional and translational feedback loops (E-box, D-box, and RORE)
334 of the circadian clock [7] and the KEGG mouse circadian rhythm pathway. Specifically, ARNTL and CLOCK form
335 a heterodimer that binds to the E-box in the CREs of *Per1* , activating its transcription [81]. RORA acts as a
336 transcriptional activator by binding to the RORE motifs to regulate the expression of *Npas2* [82]. Furthermore, DBP,
337 a PAR bZip TF, activates transcription of *Per* genes through its binding to the D-box in their promoter regions,
338 consistent with a previous report [83].
339
340 We further zoomed into two trios consisting of ARNTL and CLOCK as the TFs, *Nr1d1* as the target gene, and
341 two CREs located at the promoter and ~20Kb downstream of *Nr1d1* (**Fig. 5C**). While ARNTL and CLOCK have
342 been shown to regulate *Nr1d1* [84], we pinpointed a proximal and a distal CRE, in which the TFs bind at the E-box
343 element, respectively. ChIP-seq of ARNTL and CLOCK from mouse liver [85] confirmed their binding at both
344 CREs, exhibiting synchronous circadian patterns aligned with the identified trio (**Fig. 5C**). Capture Hi-C [86] further
345 confirmed a significantly rhythmic interaction between the distal CRE and the target gene *Nr1d1*, while resolution
346 was limited for the proximal CRE due to its location within the gene's promoter region (**Fig. 5C**). Moreover,
347 *Nr1d1*'s expression and rhythmicity were both depleted when ARNTL was knocked out [87] (**Fig. 5C**). Zoomed-in
348 coverage plots of the *Nr1d1* and CRE regions are shown in **Fig. 5D**, revealing that the predicted CREs were highly
349 accessible, bound by the identified TFs, and enriched with active histone marks. Additionally, our results suggest
350 that *Arntl* itself is regulated by multiple TFs, including MEF2D [88], PPARD [65], NR5A2 [86], and NFYB [89], consistent
351 with previous reports (**Fig. S23**). These findings underscore the complex and multifaceted regulatory network
352 governing clock gene expression, highlighting their critical role in circadian rhythm regulation.
353
354 Further examination of the identified CRE-TF-gene trios reveals a strong correlation between the phases of CRE
355 accessibility and the phases of the target gene expression, although both can be out of phase with the TF regulator.

356 See **Fig. 5E** for two sets of trios with ARNTL and NR1D1 as the TF regulators, respectively. We show that the
357 binding of the TF regulators is asynchronous with the expression of the target genes they regulate, consistent with
358 previous reports [47,90]. By incorporating the additional ATAC modality, we provide evidence that the target gene
359 expression, in addition to being regulated by TFs, is also governed by a linked CREs with synchronized
360 accessibilities (**Fig. 5E**). This suggests a finely tuned regulatory system, where both TFs and chromatin states
361 coordinate to ensure precise circadian gene expression control.
362
363 Gene regulatory networks for the core clock and clock reference genes were further constructed, including the E-
364 box binding TFs (ARNTL, CLCOK, and NPAS2), the RORE binding TFs (RORA, RORC, and NR1D1), the D-
365 box binding TF (DBP), and TFs without annotated binding motifs (PER1, PER2, and CRY1) (**Fig. S24**). The
366 reconstructed regulatory network is highly consistent with the KEGG circadian rhythm pathway, and we further
367 validated it using chromatin-state annotation, promoter capture Hi-C, and TF ChIP-seq (**Fig. 5F**). Specifically,
368 the predicted CREs were enriched at TSSs and enhancers but depleted in quiescent regions compared to random
369 peaks. Hypergeometric tests demonstrated that the identified CREs were significantly enriched for peak-gene
370 interactions. Furthermore, TFs that are predicted to bind at CREs showed significantly higher ChIP-seq signals
371 for ARNTL, CLOCK, and NPAS2 compared to random peaks.
372
373 **DISCUSSION**
374 Recent advances in next-generation sequencing technologies offer appealing platforms to identify circadian genes
375 and elucidate the mechanisms that regulate their rhythmic expression [17,18]. Traditional bulk-tissue sequencing
376 pools thousands to millions of cells with an averaged readout, masking the intricate cellular diversity by blending
377 various cell types and states. To date, several scRNA-seq studies have measured cellular gene expression at
378 different time points across the 24-hour cycle [25-28]. However, to the best of our knowledge, this study is the first
379 to generate a single-cell multiomics dataset that simultaneously measures gene expression and chromatin
380 accessibility to investigate circadian rhythmicity. This new technology brings distinct advantages, poised to
381 challenge the existing status quo.
382
383 Specifically, this time-series single-cell multiomic design allows us to systematically characterize and disentangle
384 the different levels of heterogeneity: between discretized cell types and transient cell states, across circadian
385 timepoints and spatial locations, and among different genomic modalities simultaneously measured within the
386 same cells. Mouse liver comprises diverse cell types such as hepatocytes, Kupffer cells, fibroblasts, endothelial
387 cells, T cells, and B cells [29]. Moreover, the hepatocytes exhibit pronounced subtype specificity due to the liver's
388 anatomical compartmentalization into lobules [71]. We identified cell-type-specific molecular "clocks" across
389 different modalities and demonstrated that hepatocytes displayed the most pronounced and robust cyclic patterns.

390 Additionally, we examined omics profiles across spatial zonation and revealed not only circadian but also spatial
391 and spatiotemporal gene expressions and regulatory relationships. Notably, while we computationally
392 reconstructed the PN-to-CV trajectory using well-established methods, we did not properly account for the
393 inference uncertainty. Looking ahead, applying recently developed imaging- and sequencing-based spatial
394 transcriptomics technologies – particularly those with subcellular resolution, such as 10x Genomics' Xenium and
395 Visium HD platforms – will allow direct and unbiased measures of the spatial location.
396
397 We demonstrate on the genome-wide scale that the fractions of bursting cells (i.e., cells with non-zero expressions
398 in the scRNA-seq) closely recapitulates the rhythmic patterns of the averaged expressions, as traditionally
399 measured in bulk RNA-seq. This regulation by burst frequency, instead of burst size, has previously been shown
400 to take effect in core clock genes [33,66], as well as in several other contexts: across different genes [91], during the
401 cell cycle [92], under different growth condition [93], through regulation by TFs [94], and via looped contacts between
402 enhancers and promoters [66,95]. Importantly, we show that the bursting fractions are strongly correlated with the
403 Gini index and the coefficient of variation, suggesting that "noise" or variation resulting from stochastic
404 transcription also exemplify robust rhythmicity. It is worth noting that while a two-state Poisson-Beta model [31,70]
405 has been proposed to infer the bursting kinetics, in this study, we resorted to the fraction of bursting cells as a
406 surrogate measure of burst frequency and the non-zero mean expression as a surrogate measure of burst size. This
407 is primarily due to the highly sparse and noisy data from 10x Genomics' 3' end tagging, which led to poor model
408 fitting with identifiability issues [31,96]. The inherent heterogeneity within the same cell type (e.g., across different
409 spatial zonation and circadian time points) further exacerbated the problem, necessitating a large number of cells
410 for accurate parameter estimation. With recent developments of full-transcript scRNA-seq [97,98], we anticipate
411 more accurate estimates of both burst frequency and burst size, potentially at isoform and allele resolution, which
412 will help further disentangle the various components of circadian regulation by transcriptional bursting.
413
414 To infer the transcriptional regulation of circadian gene expression, we conducted a genome-wide scan, focusing
415 on one CRE-TF-gene trio at a time. It is important to note that this CRE-TF-gene conditional association does not
416 imply causation, nor does it account for other TF regulators or mediators that may also be involved in this complex
417 regulatory network. With increased data resolution and cell numbers, it would be meaningful to explore beyond
418 the marginal and trio relationships to incorporate higher-order models possibly with variable selection that can
419 more realistically capture the complex regulatory relationships between multiple CREs, modules consisting of
420 multiple TFs, and target gene expression. The abundance of data from past and ongoing bulk sequencing studies,
421 coupled with the maturation of single-cell sequencing protocols, can also be further exploited via a joint
422 deconvolution framework [99] that utilizes cellular level rhythmic profiles to uncover cell-type and cell-state
423 contributions in circadian biology.

Last but not least, an interesting observation we want to highlight is that our ATAC fragments showed significant TSS enrichment from ZT02 to ZT06 (**Fig. S25**). While TSS enrichment is typically a QC metric to filter out cells that have failed library preparations and sequencing [100], validation using published ChIP-seq data of RNA polymerase II (Pol II), TATA-binding protein (Tbp, responsible for Pol II loading and initiation [101]), Negative Elongation Factor A (Nelf-A, responsible for stablizing Pol II [101]), and H3K4me3 histone modification confirmed heightened TSS enrichment at ZT02 (**Fig. S25**). These findings provide deeper insights into the complex role of RNA polymerase II pausing in regulating the temporal dynamics of gene transcription in the mouse liver [101,102].

ACKNOWLEDGEMENTS

This work was supported by the Swiss National Science Foundation Grant 310030B_201267 (to F.N.), the National Institute of Health (NIH) Grants R01 DK128133 (to J.M.), R01 GM145737 (to J.M.), and R35 GM138342 (to Y.J.). The authors thank Drs. Dingbang Ma and Michael Roshbash for providing support on the *Drosophila* neuron data, Drs. Shao'ang Wen and Jun Yan for providing support on the mouse SCN data, Chaohua Wu for helping with ImageJ, and High Performance Research Computing at Texas A&M University for providing computational resources and support.

AUTHOR CONTRIBUTIONS

J.M. and Y.J. initiated and envisioned the study. A.J., X.N., C.R.G., and J.M. performed the mouse experiments; C.H. and F.N. generated the smFISH data. All authors performed data analysis and results interpretation. C.Y.T. and Y.J. wrote the manuscript, which was reviewed and approved by all authors.

DECLARATION OF INTERESTS

The authors declare no competing interests.

448 **KEY RESOURCES TABLE**

REAGENT or RESOURCE	SOURCE	IDENTIFIER
Deposited data		
Time-series single-cell RNA + ATAC multiomics of mouse liver	This paper	GEO: GSE288579
Time-series ChIP-seq data of Pol II, Tbp, and Nelf-A of mouse liver	Zhu et al. [101]	GEO: GSE96773
Time-series ChIP-seq of H3K4me3 and K3K36me3 of mouse liver	Le Martelot et al. [102]	GEO: GSE35790
Reference scRNA-seq data of mouse liver	Liver Cell Atlas [29]	https://livercellatlas.org
Time-series bulk-tissue RNA-seq of 1096 mouse liver samples from 57 public datasets	Brooks et al. [35]	https://zenodo.org/records/7760579
Time-series bulk-tissue GRO-seq of mouse liver	Fang et al. [47]	GEO: GSE59486
Time-series bulk-tissue Nascent-seq of mouse liver	Menet et al. [48]	GEO: GSE36872
Time-series bulk-tissue RNA-seq of mouse liver	Menet et al. [48]	GEO: GSE36871
Mouse brain suprachiasmatic nucleus (SCN) scRNA-seq	Wen et al. [25]	GEO: GSE117295
Drosophila brain clock neurons scRNA-seq	Ma et al. [26]	GEO: GSE157504
H3K27ac and H3K4me1 ChIP-seq of mouse liver	ENCODE [77]	GEO: GSE29184
Time-series ARNTL ChIP-seq of mouse liver	Koike et al. [85]	GEO: GSE39977
Time-series capture Hi-C of mouse liver	Furlan-Magaril et al. [86]	GEO: GSE155161
Time-series WT v.s. Arntl KO transcriptomics of mouse liver	Atger et al. [103]	GEO: GSE73554
ARNTL, CLOCK, and NPAS2 ChIP-seq of mouse liver	Koike et al. [85]	GEO: GSE39977

Software and algorithms		
Original source code	This paper	https://github.com/yuchaojiang/circadian_sc_multiomics
Cell Ranger	Satpathy et al. [104]	https://www.10xgenomics.com/support/software/cell-ranger
Seurat	Stuart et al. [42]	https://satijalab.org/seurat
Signac	Stuart et al. [100]	https://stuartlab.org/signac
scDblFinder	Germain et al. [105]	https://github.com/plger/scDblFinder
JTK_CYCLE / MetaCycle	Hughes et al. [51] and Wu et al. [52]	https://github.com/gangwug/MetaCycle
Heavy-tailed combination test	Gui et al. [54]	https://github.com/gl-ybnbxb/heavytailcombtest
CircaCompare	Parsons et al. [58]	https://github.com/RWParsons/circacompare
TRIPOD	Jiang et al. [41]	https://github.com/yuchaojiang/TRIPOD
ChromVar	Schep et al. [43]	https://github.com/GreenleafLab/motifmatchr
Destin2	Guan et al. [44]	https://github.com/yuchaojiang/Destin2
JASPAR	Rauluseviciute et al. [61]	https://jaspar.elixir.no
ClusterProfiler	Xu et al. [106]	https://github.com/YuLab-SMU/clusterProfiler
PSEA	Zhang et al. [56]	https://github.com/ranafi/PSEA

449

450 **METHODS**

451 **Mouse liver tissue collection**

452 Experiments with mice were approved by the Texas A&M University Institutional Animal Care and Use
453 Committee. Wild type adult males (C57BL/6NCrl strain; Charles River laboratories) were single housed under
454 12 h light:12 h dark and provided food and water *ad libitum*. Mice were euthanized by isoflurane anesthesia
455 followed by decapitation, with four biological replicates combined at each timepoint for library preparation and
456 sequencing. Livers were dissected quickly after euthanasia, briefly washed in ice-cold 1X PBS, snap-frozen in
457 liquid nitrogen, and stored at -80ºC until nuclei purification.

458

459 **Single-Cell RNA + ATAC Multiomics**

460 Nuclei isolation, library preparation, and sequencing of flash-frozen mouse liver tissue samples were performed
461 at Singulomics Corporation (https://singulomics.com; Bronx, NY). Flash-frozen mouse liver tissue samples were
462 processed to isolate nuclei using a combination of lysis, purification, and permeabilization steps. Nuclei were
463 prepared by homogenizing the tissue in a lysis buffer, followed by filtration and resuspension in diluted nuclei
464 buffer optimized for subsequent steps. This buffer formulation, containing magnesium and RNase inhibitors,
465 ensured compatibility with downstream transposition and barcoding processes.

466

467 Purified nuclei were subjected to transposition in a reaction mix containing transposase, which preferentially
468 fragmented open-chromatin regions and appended adapter sequences to the ends of DNA fragments.
469 Polyadenylated RNA molecules within the nuclei were reverse-transcribed into full-length cDNA. These
470 processes occurred within nanoliter-scale Gel bead-in-EMulsion (GEM), generated using the Chromium Next
471 GEM platform. Each GEM contained the necessary reagents for DNA and RNA barcoding, ensuring unique
472 molecular and nucleus-specific indexing.

473

474 Following GEM incubation, barcoded DNA and cDNA were recovered, purified, and amplified via PCR to
475 generate sufficient material for library construction. ATAC libraries underwent size selection, while cDNA for
476 gene expression libraries was enzymatically fragmented, end-repaired, and adapter-ligated prior to further
477 amplification. Both libraries were subjected to QC to ensure high fidelity. Sequencing of the final libraries was
478 performed on an Illumina NovaSeq platform using paired-end 150 bp reads (PE150), targeting a depth of ~200
479 million reads per library.

480

481 **Demultiplexing, quantification, and quality control**

482 Sequencing reads were analyzed with mouse reference genome mm10 using Cell Ranger [104,107] ARC 2.0.2.
483 Aggregation of the samples was performed using the cellranger-arc aggr function, which subsampled from higher

484 depth GEM wells until it equalized the median number of unique fragments per cell for each ATAC library and
485 the mean number of reads mapped to the transcriptome per cell for each gene expression library. In addition to
486 gene expression from the RNA assay and chromatin accessibility from the ATAC assay, we further utilized Signac
487 [100] and chromVAR [43] to derive ATAC gene activity and motif score, respectively. Specifically, gene activity score
488 [42] computes ATAC read counts per cell in the gene body and promoter region (2 Kb upstream of TSS), while
489 motif deviation score [43] quantifies the overall accessibility within peaks sharing the same TF-binding motif while
490 controlling for other technical biases.
491
492 We used scDblFinder [105] to remove cell doublets from both the RNA and ATAC modalities. We further adopted
493 the following QC criteria and required each cell to have: (i) total number of reads between 1,000 and 100,000 for
494 both RNA and ATAC, (ii) more than 500 detected features (genes and peaks), (iii) a TSS enrichment score
495 between 3 and 20, (iv) a nucleosome signal below 2, and (v) mitochondrial read percentage under 5% (**Fig. S2**).
496 These stringent thresholds ensure the inclusion of high-quality cells and features for downstream analysis. After
497 QC, we retained a total of 33,510 cells with genome-wide measurements of 16,369 genes and gene activities,
498 149,302 peaks, and 746 motifs.
499
500 **Data normalization and integration**
501 For data normalization, we applied different methods for each modality: RNA gene expression was normalized
502 using sctransform, ATAC peak accessibility was normalized with Latent Semantic Indexing (LSI), and ATAC
503 gene activity was normalized using logNormalize. Specifically, sctransform utilizes regularized negative binomial
504 regression to normalize UMI count data. This approach effectively mitigates technical variability, such as
505 differences in sequencing depth, while preserving biological heterogeneity. LSI applies term frequency-inverse
506 document frequency (TF-IDF) for normalization, followed by singular value decomposition (SVD), correcting
507 for differences in sequencing depth while retaining biologically meaningful variations. Log normalization of gene
508 activity scores stabilizes variance, mitigates skewness, and enhances comparability across genes and cells. Motif
509 deviation score is calculated by computing the difference between the observed number of fragments mapped to
510 peaks containing the motif and the expected number, adjusting for technical confounders including GC content
511 and the mean accessibility of the peak set [43]. We used the the z-scores returned by chromVAR for each TF-binding
512 motif in each cell.
513
514 Data integration was first performed across different time points within each modality for RNA gene expression,
515 ATAC peak accessibility, ATAC gene activity, and motif deviation score, respectively (**Fig. S3**). Specifically, for
516 each pair of datasets collected at two time points, we first identified "anchors", consisting of two cells (with one
517 cell from each time point) that were predicted to originate from a common biological state. An anchor score and

518 weight were subsequently calculated, which were used for batch-effect correction using the technique adopted by
519 the mutual nearest neighbor method [108]. This procedure was iteratively performed to merge all six time points,
520 ensuring that the integrated data accurately reflect biological differences while minimizing technical artifacts. We
521 further carried out between-modality data integration to borrow information from different modalities using
522 multiCCA [44] (**Fig. 1B**), a statistical method designed to identify shared patterns among multiple datasets.
523 MultiCCA operates by finding linear combinations of variables within each dataset that are maximally correlated
524 with those in other datasets, effectively capturing common sources of variation. This approach enables the
525 alignment of distinct data types, such as RNA gene expression and ATAC peak accessibility.
526

527 **Annotating cell types, reconstructing metacells, and mapping spatial zonation**

528 Cell-type annotations were transferred from the LCA [29], enabling the identification of hepatocytes, endothelial
529 cells, fibroblasts, Kupffer cells, cholangiocytes, B cells, and T cells (**Fig. S4**). To ensure equal testing power
530 across cell types that have different numbers of cells, we downsampled hepatocytes, endothelial cells, fibroblasts,
531 and Kupffer cells to the same cell count for each cell type at each time point. We then performed cell-wise
532 smoothing by pooling similar cells into metacells [109], representing distinct cell types and states. To determine the
533 optimal resolution for metacell reconstruction, we used a list of 104 rhythmic and 113 arrhythmic genes [50] in
534 mouse liver as positive and negative controls to generate the receiver operating characteristic (ROC) curve. The
535 analysis indicated that a resolution of 2.5 yielded an area under the curve (AUC) greater than 0.8 for both RNA
536 expression and ATAC activity (**Fig. S8**). The downsampling and cell aggregation procedures were repeated 20
537 times to ensure robustness and reproducibility of the results. To reconstruct the features for the metacells, we
538 either took the average or calculated the fraction of cells with non-zero measures. Slingshot [73] was used to
539 reconstruct the PN-to-CV trajectory and to infer pseudotime for each hepatocyte in the compartmentalized liver
540 lobules. For simplified visualization, we further grouped the metacells into six spatial zones based on their inferred
541 pseudotime.
542

543 **Circadian rhythm detection**

544 To detect rhythmicity of RNA expression, ATAC activity and motif score, we applied both JTK_CYCLE [51]
545 (implemented in MetaCycle [52]) and harmonic regression [53]. We combined the resulting nominal p-values using a
546 heavy-tailed combination test [54] and adopted the Benjamini-Hochberg method for multiple testing correction (q-
547 value < 0.05). Phases were estimated through harmonic regression [53]. Gene ontology enrichment analyses using
548 cell-type-specific rhythmic genes were performed using clusterProfiler [106]. We used PSEA [56] to identify phase-
549 clustered functional enrichment using genes with cyclic RNA expression and CircaCompare [58] to test for
550 significant phase shifting between different cyclic modalities. Motif enrichment analysis rhythmic ATAC peaks

551 (q-value <0.05) was carried out using Signac [100] and JASPAR [61]. Rhythmicity of bursting fraction and its
552 comparison against that of mean expression in hepatocytes is calculated in a similar fashion.
553
554 **smFISH imaging, processing, and quantification**
555 *Arntl* and *Per1* smFISH data were generated as previously described [66] on fresh-frozen liver cryosections (8 µm
556 thick) embedded in O.C.T. Compound (Tissue-Tek; Sakura-Finetek), sampled every 3 hours from ZT00 to ZT21.
557 RNAscope probes targeting *Arntl* (#438741) and *Per1* (#438751) were used according to the manufacturer's
558 protocol for the RNAscope Fluorescent Multiplex V1 Assay (ACDBio). Newly generated smFISH data against
559 *Agxt* was obtained from formalin-fixed paraffin-embedded (FFPE) liver sections (8 µm thick). Liver lobes were
560 collected every 4 hours (ZT00 to ZT20) and fixed in 10% neutral buffered formalin (NBF) at 4°C for 24 to 36
561 hours. smFISH was performed using the RNAscope Fluorescent Multiplex V2 Assay (ACDBio) following the
562 manufacturer's instructions, with the probe targeting *Agxt* (#525261). Sections were counterstained with DAPI.
563
564 Imaging was conducted with a Leica DM5500 widefield microscope equipped with an oil-immersion ×63
565 objective lens. Z-stacks were acquired with 0.2 µm intervals. mRNA transcripts were quantified using ImageJ.
566 Nuclei were detected through a series of image processing steps, including filtering to enhance features,
567 thresholding to segment nuclei from the background, and watershed transformation to separate closely adjacent
568 nuclei. PN and CV were manually annotated based on the presence or absence of the bile duct, as determined by
569 DAPI staining. To detect fluorescent RNA-FISH spots, a Gaussian mixture model with two components was
570 implemented to select only the larger dots colocalized with the genes in cell nuclei, ensuring accurate counting
571 and an enhanced signal-to-noise ratio (**Fig. S26**). The total number of nuclei in each image was counted, and
572 mRNA concentration was calculated as $\log_2$ of the total number of nuclear smFISH transcripts divided by the
573 total number of nuclei. The bursting fraction was calculated as the number of nuclei with active transcription
574 divided by the total number of nuclei. Regions were selected for zoomed-in visualization at each ZT.
575
576 **Varying coefficient model for spatiotemporal analysis**
577 We propose a statistical framework to test whether RNA expression (or ATAC activity) exhibits a significant
578 spatial, circadian, or combined spatial and circadian pattern across spatial zonation and/or circadian time points,
579 focusing on one gene at a time. For cell i, let y_i be its gene expression, t_i be its ZT time point of collection, and
580 p_i be its pseudotime along the spatial gradient. We test one gene at a time and thus remove the gene index in the
581 following models. Specifically, the null model H_0 is specified as $y_i = C + \epsilon_i$, where C denotes the baseline gene
582 expression with error term $\epsilon_i \sim N(0, \sigma^2)$. The circadian model H_1 is specified as a cosinor curve [110] of form $y_i =$
583 $C + E\sin(\omega t_i) + F\cos(\omega t_i) + \epsilon_i$. For the spatial model H_2, we carried out a basis expansion (polynomial of
584 degree three by default) of the pseudotime to account for any nonlinear relationship $y_i = \sum_k C_k \phi_k(p_i) + \epsilon_i$.

585 Lastly, for the spatial and circadian model H_3, we adopted a varying-coefficient model of form $y_i =$
586 $\sum_k C_k \phi_k(p_i) + \sum_k E_k \phi_k(p_i) \sin(\omega t_i) + \sum_k F_k \phi_k(p_i) \cos(\omega t_i) + \epsilon_i$, where the coefficients from the cosinor
587 model are functions of the pseudotime upon basis expansions. We fit each of the four models and adopt likelihood
588 ratio statistics for testing. Null log likelihood ratio statistics follows a chi-squared distribution; we perform a
589 likelihood ratio test with finite-sample adjustments [111] to avoid inflated type I error.
590
591 **Linking spatiotemporal CREs to target genes**
592 Hepatocytes are grouped by time points (ZT02, ZT06, ZT10, ZT14, ZT18, ZT22) or zonation (zones 1 to 6) and
593 randomly sampled without replacement to reconstruct four replicates per time point or zone, ensuring equal testing
594 powers. We calculate the mean RNA expression and mean ATAC peak accessibility for each group and scan for
595 significant association between a target gene and a peak region located within 500 Kb of the gene's TSS via a
596 correlation-based test. A circadian CRE is linked to a circadian gene across circadian timepoints with a significant
597 correlation coefficient greater than 0.5. Similarly, a spatial CRE is linked to a spatial gene across spatial zonation
598 with a significant correlation coefficient greater than 0.5. A spatial and circadian CRE is linked to a spatial and
599 circadian gene with correlation coefficients significantly exceeding 0.5 under both contexts.
600
601 **CRE-TF-gene regulatory trios in circadian control**
602 Metacell-specific omics profiles were used as input for TRIPOD [41], a nonparametric computational framework
603 designed to analyze single-cell multiomic data and identify regulatory relationships between CREs, TFs, and
604 target genes. The candidate CRE regions are defined as 200 Kb upstream and downstream of the TSSs. An q-
605 value threshold of 0.01 was adopted to assess significance. The results from TRIPOD were further validated
606 through chromatin-state annotation, promoter capture Hi-C, and TF ChIP-seq, demonstrating the robustness of
607 the findings.
608
609 **DATA AND CODE AVAILABILITY**
610 Raw and processed single-cell RNA and ATAC multiomic data from this study have been deposited at GEO
611 (https://www.ncbi.nlm.nih.gov/geo) under the accession number GEO: GSE288579. All original code is publicly
612 available at the GitHub repository https://github.com/yuchaojiang/circadian_sc_multiomics.

613 **FIGURE LEGENDS**

614 **Fig. 1. Single-nucleus RNA expression and chromatin accessibility multiomic analysis of mouse liver over**
615 **a 24-hour cycle.** (A) Experimental design. Mouse liver tissues were collected from wild type mice at six circadian
616 time points and processed using the 10x Genomics Chromium Single Cell Multiome platform, enabling
617 simultaneous measurement of RNA expression and chromatin accessibility in the same cells. Liver tissues from
618 four male mice were pooled in equal proportions per time point to minimize inter-mouse variability. (B) Within-
619 modality UMAP dimension reduction of RNA expression, ATAC peak accessibility, ATAC gene activity, motif
620 deviation score, and cross-modality integration using MultiCCA. (C) RNA and ATAC profiles of previously
621 reported cell-type-specific marker genes. (D) Pseudo-bulk RNA and ATAC profiles recapitulate rhythmicity of
622 previously identified circadian genes (top 2000 cyclic genes from Hughes et al. [46]). All cells were combined to
623 generate pseudo-bulk samples, with average RNA expression and ATAC activity calculated.

624

625 **Fig. 2. Rhythmic RNA expression and ATAC activity vary across liver cell types and are the most**
626 **pronounced in hepatocytes.** (A) Dot plots show the average RNA expression and ATAC activity (dot color) and
627 the percentage of cells with non-zero RNA expression and ATAC activity (dot size) for core clock and clock
628 reference genes across time points and cell types. Statistically significant rhythmicities are marked with asterisks.
629 To ensure equal testing power, hepatocytes, endothelial cells, fibroblasts, and Kupffer cells were downsampled
630 to the same number of cells. (B) Upset plots depict the gene overlap of cell-type-specific rhythmicity for both
631 RNA expression and ATAC activity (q-value < 0.05), highlighting hepatocytes as the primary contributors to
632 liver rhythmicity. (C) Phase set enrichment analysis identified phase-clustered gene ontologies in different cell
633 types. (D) Gene overlap of rhythmic RNA expression and ATAC activity in hepatocytes. (E) Phases of RNA
634 expression and ATAC activity are highly correlated. We tested for significant phase shifts between the two
635 modalities using CircaCompare [58]. (F) Representative clock genes were visualized: *Arntl* and *Npas2* exhibit
636 synchronized rhythmicity between RNA and ATAC modalities, while ATAC activity of *Per1*, *Clock*, and *Nr1d1*
637 shows a significant priming effect relative to their RNA expression. (G) Genes with significantly smaller ATAC
638 phases compared to RNA are longer and exhibit larger relative amplitude (rAMP). (H) Phase-specific TF-binding
639 motifs significantly enriched in cyclic ATAC peaks. Representative phase-clustered motifs are visualized with
640 position weight matrices and adjusted p-values.

641

642 **Fig. 3. Moving beyond mean measurements: rhythmic nuclear gene expression driven by rhythmic**
643 **bursting fraction.** (A) Two models of circadian rhythmicity: one driven by the average expression across cells
644 and the other by the fraction of bursting cells with non-zero transcripts. (B) Core clock and clock reference genes
645 exhibit nearly identical cyclic patterns of both mean expression and bursting fraction. (C) Venn diagram depicting
646 the gene overlap between rhythmicity detected by mean expression and bursting fraction. (D) Boxplot of RNA

647 expression for cyclic genes identified by mean expression and bursting fraction. Cyclic genes identified by mean
648 expression have significantly higher fractions of cells in the "ON" bursting state and significantly higher absolute
649 expression levels. (E) Correlations of adjusted p-values (left), amplitudes (middle), and phases (right) between
650 rhythmicity detected by mean expression and bursting fraction. Results are reproduced using time-series scRNA-
651 seq data from mouse SCN [25] and *Drosophila* neuron [26]. (F) Orthogonal and experimental validation by smFISH
652 of *Arntl* and *Per1* in mouse liver at different time points [27]. Mean RNA concentration and proportion of nuclei
653 with non-zero transcripts show near-identical cyclic patterns.
654
655 **Fig. 4. Spatiotemporal gene expression and regulation across lobular zonation and circadian time points.**
656 (A) Schematic of the liver lobule, where concentric layers of hepatocytes are positioned along PN-to-CV axis.
657 Blood flow and secreted morphogens give rise to a spatially graded microenvironment, resulting in different
658 functions assigned to different zonation. (B) UMAP dimension reduction of hepatocytes colored by inferred
659 pseudotime. (C) Spatial distribution of RNA expression and ATAC activity for two marker genes, *Cyp2f2* and
660 *Cyp2e1*, enriched at the PN and CV, respectively. (D) Venn diagram of circadian, spatial, and spatial and circadian
661 genes detected. (E) Visualization of a circadian gene *Arntl* and a spatial gene *Glul*. (F) Visualization of spatial
662 and circadian genes, validated by smFISH. (G) Newly identified spatial and circadian gene *Agxt*, validated by
663 newly generated smFISH data. Red dots represent *Agxt* transcripts; purple shapes represent cell nuclei. (H)
664 Representative CREs regulating circadian and/or spatial expression of target genes. Cells are grouped by either
665 circadian time points or spatial zonation. Enriched motifs are identified from each target genes' significantly
666 linked CREs and are consistent with previous reports. (I) Number of CREs that regulate circadian rhythms, spatial
667 expression, or both simultaneously. (J) ChIP-seq of H3K27ac and H3K4me1 [77], active enhancer markers, for
668 circadian, spatial, and combined spatial and circadian CREs, compared to random regions from the mouse genome.
669 (K) Illustration of CREs significantly linked to target genes regulating circadian rhythmicity, spatial variation, or
670 both.
671
672 **Fig. 5. Transcriptional control of rhythmic gene expression in hepatocytes.** (A) Schematic of a CRE-TF-gene
673 trio: a TF binds at a CRE to regulate target gene expression. (B) Significant trios consistent with prior knowledge,
674 including the transcription-translation feedback loops for circadian control and the mouse circadian KEGG
675 pathway. (C) ARNTL and CLOCK bind to CREs to regulate *Nr1d1* gene expression [84]. Validation includes time-
676 series ChIP-seq data confirming ARNTL and CLOCK binding at the CREs [85], as well as time-series capture Hi-
677 C data confirming CRE-*Nr1d1* interaction [86]. *Nr1d1* expression and rhythmicity are depleted upon *Arntl* knockout.
678 (D) Zoomed-in coverage plots of scRNA-seq, scATAC-seq, TF ChIP-seq (ARNTL and CLOCK), DNase-seq,
679 and histone ChIP-seq at the predicted proximal and distal CREs and the target gene. (E) Trios involving ARNTL
680 (left) and NR1D1 (right) as TFs. While phases of the target genes and their CREs are highly correlated, they can

681 be out-of-phase with their regulating TFs. This aligns with findings that enhancer RNAs play an essential role in
682 controlling target gene rhythmicity, which is anti- or out-of-phase with TF binding rhythmicity [47]. (F) Chromatin-
683 state annotation of linked CREs, capture Hi-C validation of CRE-gene interactions [86], and ChIP-seq validation of
684 CRE-TF linkage [85]. Compared to random genomic regions, identified CREs are enriched at TSSs and enhancers,
685 exhibit statistically significant interactions with target genes, and show a markedly higher frequency of TF binding.

686 **REFERENCES**

687 1. Pittendrigh, C.S. (1960). Circadian rhythms and the circadian organization of living systems. Cold Spring
688 Harb Symp Quant Biol *25*, 159-184. 10.1101/sqb.1960.025.01.015.
689 2. Freedman, M.S., Lucas, R.J., Soni, B., von Schantz, M., Munoz, M., David-Gray, Z., and Foster, R. (1999).
690 Regulation of mammalian circadian behavior by non-rod, non-cone, ocular photoreceptors. Science *284*,
691 502-504. 10.1126/science.284.5413.502.
692 3. Lamia, K.A., Storch, K.F., and Weitz, C.J. (2008). Physiological significance of a peripheral tissue
693 circadian clock. Proc Natl Acad Sci U S A *105*, 15172-15177. 10.1073/pnas.0806717105.
694 4. Panda, S. (2016). Circadian physiology of metabolism. Science *354*, 1008-1015. 10.1126/science.aah4967.
695 5. Dunlap, J.C. (1999). Molecular bases for circadian clocks. Cell *96*, 271-290. 10.1016/s0092-
696 8674(00)80566-8.
697 6. Kim, Y.H., and Lazar, M.A. (2020). Transcriptional Control of Circadian Rhythms and Metabolism: A
698 Matter of Time and Space. Endocr Rev *41*, 707-732. 10.1210/endrev/bnaa014.
699 7. Takahashi, J.S. (2017). Transcriptional architecture of the mammalian circadian clock. Nat Rev Genet *18*,
700 164-179. 10.1038/nrg.2016.150.
701 8. Shearman, L.P., Sriram, S., Weaver, D.R., Maywood, E.S., Chaves, I., Zheng, B., Kume, K., Lee, C.C.,
702 van der Horst, G.T., Hastings, M.H., and Reppert, S.M. (2000). Interacting molecular loops in the
703 mammalian circadian clock. Science *288*, 1013-1019. 10.1126/science.288.5468.1013.
704 9. Preitner, N., Damiola, F., Lopez-Molina, L., Zakany, J., Duboule, D., Albrecht, U., and Schibler, U. (2002).
705 The orphan nuclear receptor REV-ERBalpha controls circadian transcription within the positive limb of
706 the mammalian circadian oscillator. Cell *110*, 251-260. 10.1016/s0092-8674(02)00825-5.
707 10. Mitsui, S., Yamaguchi, S., Matsuo, T., Ishida, Y., and Okamura, H. (2001). Antagonistic role of E4BP4
708 and PAR proteins in the circadian oscillatory mechanism. Genes Dev *15*, 995-1006. 10.1101/gad.873501.
709 11. Patke, A., Murphy, P.J., Onat, O.E., Krieger, A.C., Ozcelik, T., Campbell, S.S., and Young, M.W. (2017).
710 Mutation of the Human Circadian Clock Gene CRY1 in Familial Delayed Sleep Phase Disorder. Cell *169*,
711 203-215 e213. 10.1016/j.cell.2017.03.027.
712 12. Li, J.Z., Bunney, B.G., Meng, F., Hagenauer, M.H., Walsh, D.M., Vawter, M.P., Evans, S.J., Choudary,
713 P.V., Cartagena, P., Barchas, J.D., et al. (2013). Circadian patterns of gene expression in the human brain
714 and disruption in major depressive disorder. Proc Natl Acad Sci U S A *110*, 9950-9955.
715 10.1073/pnas.1305814110.
716 13. Kettner, N.M., Voicu, H., Finegold, M.J., Coarfa, C., Sreekumar, A., Putluri, N., Katchy, C.A., Lee, C.,
717 Moore, D.D., and Fu, L. (2016). Circadian Homeostasis of Liver Metabolism Suppresses
718 Hepatocarcinogenesis. Cancer Cell *30*, 909-924. 10.1016/j.ccell.2016.10.007.
719 14. Guan, D., Xiong, Y., Borck, P.C., Jang, C., Doulias, P.T., Papazyan, R., Fang, B., Jiang, C., Zhang, Y.,
720 Briggs, E.R., et al. (2018). Diet-Induced Circadian Enhancer Remodeling Synchronizes Opposing Hepatic
721 Lipid Metabolic Processes. Cell *174*, 831-842 e812. 10.1016/j.cell.2018.06.031.
722 15. Lim, A.S., Klein, H.U., Yu, L., Chibnik, L.B., Ali, S., Xu, J., Bennett, D.A., and De Jager, P.L. (2017).
723 Diurnal and seasonal molecular rhythms in human neocortex and their relation to Alzheimer's disease. Nat
724 Commun *8*, 14931. 10.1038/ncomms14931.
725 16. Zwighaft, Z., Aviram, R., Shalev, M., Rousso-Noori, L., Kraut-Cohen, J., Golik, M., Brandis, A., Reinke,
726 H., Aharoni, A., Kahana, C., and Asher, G. (2015). Circadian Clock Control by Polyamine Levels through
727 a Mechanism that Declines with Age. Cell Metab *22*, 874-885. 10.1016/j.cmet.2015.09.011.
728 17. Rijo-Ferreira, F., and Takahashi, J.S. (2019). Genomics of circadian rhythms in health and disease.
729 Genome Med *11*, 82. 10.1186/s13073-019-0704-0.
730 18. Nozue, K., Covington, M.F., Duek, P.D., Lorrain, S., Fankhauser, C., Harmer, S.L., and Maloof, J.N.
731 (2007). Rhythmic growth explained by coincidence between internal and external cues. Nature *448*, 358-
732 361. 10.1038/nature05946.
733 19. Deckard, A., Anafi, R.C., Hogenesch, J.B., Haase, S.B., and Harer, J. (2013). Design and analysis of large-
734 scale biological rhythm studies: a comparison of algorithms for detecting periodic signals in biological
735 data. Bioinformatics *29*, 3174-3180. 10.1093/bioinformatics/btt541.

20. Laloum, D., and Robinson-Rechavi, M. (2020). Methods detecting rhythmic gene expression are biologically relevant only for strong signal. PLoS Comput Biol *16*, e1007666. 10.1371/journal.pcbi.1007666.
21. Mei, W., Jiang, Z., Chen, Y., Chen, L., Sancar, A., and Jiang, Y. (2021). Genome-wide circadian rhythm detection methods: systematic evaluations and practical guidelines. Brief Bioinform *22*. 10.1093/bib/bbaa135.
22. Patel, V.R., Eckel-Mahan, K., Sassone-Corsi, P., and Baldi, P. (2012). CircadiOmics: integrating circadian genomics, transcriptomics, proteomics and metabolomics. Nat Methods *9*, 772-773. 10.1038/nmeth.2111.
23. Pizarro, A., Hayer, K., Lahens, N.F., and Hogenesch, J.B. (2013). CircaDB: a database of mammalian circadian gene expression profiles. Nucleic Acids Res *41*, D1009-1013. 10.1093/nar/gks1161.
24. Li, X., Shi, L., Zhang, K., Wei, W., Liu, Q., Mao, F., Li, J., Cai, W., Chen, H., Teng, H., et al. (2018). CirGRDB: a database for the genome-wide deciphering circadian genes and regulators. Nucleic Acids Res *46*, D64-D70. 10.1093/nar/gkx944.
25. Wen, S., Ma, D., Zhao, M., Xie, L., Wu, Q., Gou, L., Zhu, C., Fan, Y., Wang, H., and Yan, J. (2020). Spatiotemporal single-cell analysis of gene expression in the mouse suprachiasmatic nucleus. Nat Neurosci *23*, 456-467. 10.1038/s41593-020-0586-x.
26. Ma, D., Przybylski, D., Abruzzi, K.C., Schlichting, M., Li, Q., Long, X., and Rosbash, M. (2021). A transcriptomic taxonomy of Drosophila circadian neurons around the clock. Elife *10*. 10.7554/eLife.63056.
27. Droin, C., Kholtei, J.E., Bahar Halpern, K., Hurni, C., Rozenberg, M., Muvkadi, S., Itzkovitz, S., and Naef, F. (2021). Space-time logic of liver gene expression at sub-lobular scale. Nat Metab *3*, 43-58. 10.1038/s42255-020-00323-1.
28. Dopp, J., Ortega, A., Davie, K., Poovathingal, S., Baz, E.S., and Liu, S. (2024). Single-cell transcriptomics reveals that glial cells integrate homeostatic and circadian processes to drive sleep-wake cycles. Nat Neurosci *27*, 359-372. 10.1038/s41593-023-01549-4.
29. Guilliams, M., Bonnardel, J., Haest, B., Vanderborght, B., Wagner, C., Remmerie, A., Bujko, A., Martens, L., Thone, T., Browaeys, R., et al. (2022). Spatial proteogenomics reveals distinct and evolutionarily conserved hepatic macrophage niches. Cell *185*, 379-396 e338. 10.1016/j.cell.2021.12.018.
30. Halpern, K.B., Shenhav, R., Matcovitch-Natan, O., Toth, B., Lemze, D., Golan, M., Massasa, E.E., Baydatch, S., Landen, S., Moor, A.E., et al. (2017). Single-cell spatial reconstruction reveals global division of labour in the mammalian liver. Nature *542*, 352-356. 10.1038/nature21065.
31. Jiang, Y., Zhang, N.R., and Li, M. (2017). SCALE: modeling allele-specific gene expression by single-cell RNA sequencing. Genome Biol *18*, 74. 10.1186/s13059-017-1200-8.
32. Larsson, A.J.M., Johnsson, P., Hagemann-Jensen, M., Hartmanis, L., Faridani, O.R., Reinius, B., Segerstolpe, A., Rivera, C.M., Ren, B., and Sandberg, R. (2019). Genomic encoding of transcriptional burst kinetics. Nature *565*, 251-254. 10.1038/s41586-018-0836-1.
33. Nicolas, D., Zoller, B., Suter, D.M., and Naef, F. (2018). Modulation of transcriptional burst frequency by histone acetylation. Proc Natl Acad Sci U S A *115*, 7153-7158. 10.1073/pnas.1722330115.
34. Phillips, N.E., Hugues, A., Yeung, J., Durandau, E., Nicolas, D., and Naef, F. (2021). The circadian oscillator analysed at the single-transcript level. Mol Syst Biol *17*, e10135. 10.15252/msb.202010135.
35. Brooks, T.G., Manjrekar, A., Mrc ela, A., and Grant, G.R. (2023). Meta-analysis of Diurnal Transcriptomics in Mouse Liver Reveals Low Repeatability of Rhythm Analyses. J Biol Rhythms *38*, 556-570. 10.1177/07487304231179600.
36. Hor, C.N., Yeung, J., Jan, M., Emmenegger, Y., Hubbard, J., Xenarios, I., Naef, F., and Franken, P. (2019). Sleep-wake-driven and circadian contributions to daily rhythms in gene expression and chromatin accessibility in the murine cortex. Proc Natl Acad Sci U S A *116*, 25773-25783. 10.1073/pnas.1910590116.
37. Yuan, Y., Chen, Q., Brovkina, M., Clowney, E.J., and Yadlapalli, S. (2024). Clock-dependent chromatin accessibility rhythms regulate circadian transcription. PLoS Genet *20*, e1011278. 10.1371/journal.pgen.1011278.
38. Dallmann, R., Viola, A.U., Tarokh, L., Cajochen, C., and Brown, S.A. (2012). The human circadian metabolome. Proc Natl Acad Sci U S A *109*, 2625-2629. 10.1073/pnas.1114410109.

39. Masri, S., Patel, V.R., Eckel-Mahan, K.L., Peleg, S., Forne, I., Ladurner, A.G., Baldi, P., Imhof, A., and Sassone-Corsi, P. (2013). Circadian acetylome reveals regulation of mitochondrial metabolic pathways. Proc Natl Acad Sci U S A *110*, 3339-3344. 10.1073/pnas.1217632110.
40. Reddy, A.B., Karp, N.A., Maywood, E.S., Sage, E.A., Deery, M., O'Neill, J.S., Wong, G.K., Chesham, J., Odell, M., Lilley, K.S., et al. (2006). Circadian orchestration of the hepatic proteome. Curr Biol *16*, 1107-1115. 10.1016/j.cub.2006.04.026.
41. Jiang, Y., Harigaya, Y., Zhang, Z., Zhang, H., Zang, C., and Zhang, N.R. (2022). Nonparametric single-cell multiomic characterization of trio relationships between transcription factors, target genes, and cis-regulatory regions. Cell Syst *13*, 737-751 e734. 10.1016/j.cels.2022.08.004.
42. Stuart, T., Butler, A., Hoffman, P., Hafemeister, C., Papalexi, E., Mauck, W.M., 3rd, Hao, Y., Stoeckius, M., Smibert, P., and Satija, R. (2019). Comprehensive Integration of Single-Cell Data. Cell *177*, 1888-1902 e1821. 10.1016/j.cell.2019.05.031.
43. Schep, A.N., Wu, B., Buenrostro, J.D., and Greenleaf, W.J. (2017). chromVAR: inferring transcription-factor-associated accessibility from single-cell epigenomic data. Nat Methods *14*, 975-978. 10.1038/nmeth.4401.
44. Guan, P.Y., Lee, J.S., Wang, L., Lin, K.Z., Mei, W., Chen, L., and Jiang, Y. (2023). Destin2: Integrative and cross-modality analysis of single-cell chromatin accessibility data. Front Genet *14*, 1089936. 10.3389/fgene.2023.1089936.
45. Beytebiere, J.R., Trott, A.J., Greenwell, B.J., Osborne, C.A., Vitet, H., Spence, J., Yoo, S.H., Chen, Z., Takahashi, J.S., Ghaffari, N., and Menet, J.S. (2019). Tissue-specific BMAL1 cistromes reveal that rhythmic transcription is associated with rhythmic enhancer-enhancer interactions. Genes Dev *33*, 294-309. 10.1101/gad.322198.118.
46. Hughes, M.E., DiTacchio, L., Hayes, K.R., Vollmers, C., Pulivarthy, S., Baggs, J.E., Panda, S., and Hogenesch, J.B. (2009). Harmonics of circadian gene transcription in mammals. PLoS Genet *5*, e1000442. 10.1371/journal.pgen.1000442.
47. Fang, B., Everett, L.J., Jager, J., Briggs, E., Armour, S.M., Feng, D., Roy, A., Gerhart-Hines, Z., Sun, Z., and Lazar, M.A. (2014). Circadian enhancers coordinate multiple phases of rhythmic gene transcription in vivo. Cell *159*, 1140-1152. 10.1016/j.cell.2014.10.022.
48. Menet, J.S., Rodriguez, J., Abruzzi, K.C., and Rosbash, M. (2012). Nascent-Seq reveals novel features of mouse circadian transcriptional regulation. Elife *1*, e00011. 10.7554/eLife.00011.
49. Duan, J., Ngo, M.N., Karri, S.S., Tsoi, L.C., Gudjonsson, J.E., Shahbaba, B., Lowengrub, J., and Andersen, B. (2024). tauFisher predicts circadian time from a single sample of bulk and single-cell pseudobulk transcriptomic data. Nat Commun *15*, 3840. 10.1038/s41467-024-48041-6.
50. Wu, G., Zhu, J., Yu, J., Zhou, L., Huang, J.Z., and Zhang, Z. (2014). Evaluation of five methods for genome-wide circadian gene identification. J Biol Rhythms *29*, 231-242. 10.1177/0748730414537788.
51. Hughes, M.E., Hogenesch, J.B., and Kornacker, K. (2010). JTK_CYCLE: an efficient nonparametric algorithm for detecting rhythmic components in genome-scale data sets. J Biol Rhythms *25*, 372-380. 10.1177/0748730410379711.
52. Wu, G., Anafi, R.C., Hughes, M.E., Kornacker, K., and Hogenesch, J.B. (2016). MetaCycle: an integrated R package to evaluate periodicity in large scale data. Bioinformatics *32*, 3351-3353. 10.1093/bioinformatics/btw405.
53. Yang, R., and Su, Z. (2010). Analyzing circadian expression data by harmonic regression based on autoregressive spectral estimation. Bioinformatics *26*, i168-174. 10.1093/bioinformatics/btq189.
54. Gui, L., Jiang, Y., and Wang, J. (2023). Aggregating Dependent Signals with Heavy-Tailed Combination Tests. arXiv preprint arXiv:2310.20460.
55. Guan, D., Xiong, Y., Trinh, T.M., Xiao, Y., Hu, W., Jiang, C., Dierickx, P., Jang, C., Rabinowitz, J.D., and Lazar, M.A. (2020). The hepatocyte clock and feeding control chronophysiology of multiple liver cell types. Science *369*, 1388-1394. 10.1126/science.aba8984.
56. Zhang, R., Podtelezhnikov, A.A., Hogenesch, J.B., and Anafi, R.C. (2016). Discovering Biology in Periodic Data through Phase Set Enrichment Analysis (PSEA). J Biol Rhythms *31*, 244-257. 10.1177/0748730416631895.

57. Zhou, Z., Xu, M.J., and Gao, B. (2016). Hepatocytes: a key cell type for innate immunity. Cell Mol Immunol *13*, 301-315. 10.1038/cmi.2015.97.
58. Parsons, R., Parsons, R., Garner, N., Oster, H., and Rawashdeh, O. (2020). CircaCompare: a method to estimate and statistically support differences in mesor, amplitude and phase, between circadian rhythms. Bioinformatics *36*, 1208-1212. 10.1093/bioinformatics/btz730.
59. Phillips, R.A., Wan, E., Tuscher, J.J., Reid, D., Drake, O.R., Ianov, L., and Day, J.J. (2023). Temporally specific gene expression and chromatin remodeling programs regulate a conserved Pdyn enhancer. Elife *12*. 10.7554/eLife.89993.
60. Chedin, F. (2016). Nascent Connections: R-Loops and Chromatin Patterning. Trends Genet *32*, 828-838. 10.1016/j.tig.2016.10.002.
61. Rauluseviciute, I., Riudavets-Puig, R., Blanc-Mathieu, R., Castro-Mondragon, J.A., Ferenc, K., Kumar, V., Lemma, R.B., Lucas, J., Cheneby, J., Baranasic, D., et al. (2024). JASPAR 2024: 20th anniversary of the open-access database of transcription factor binding profiles. Nucleic Acids Res *52*, D174-D182. 10.1093/nar/gkad1059.
62. Sobel, J.A., Krier, I., Andersin, T., Raghav, S., Canella, D., Gilardi, F., Kalantzi, A.S., Rey, G., Weger, B., Gachon, F., et al. (2017). Transcriptional regulatory logic of the diurnal cycle in the mouse liver. PLoS Biol *15*, e2001069. 10.1371/journal.pbio.2001069.
63. Kaczynski, J., Cook, T., and Urrutia, R. (2003). Sp1- and Kruppel-like transcription factors. Genome Biol *4*, 206. 10.1186/gb-2003-4-2-206.
64. Yerra, V.G., and Drosatos, K. (2023). Specificity Proteins (SP) and Kruppel-like Factors (KLF) in Liver Physiology and Pathology. Int J Mol Sci *24*. 10.3390/ijms24054682.
65. Chen, L., and Yang, G. (2014). PPARs Integrate the Mammalian Clock and Energy Metabolism. PPAR Res *2014*, 653017. 10.1155/2014/653017.
66. Mermet, J., Yeung, J., Hurni, C., Mauvoisin, D., Gustafson, K., Jouffe, C., Nicolas, D., Emmenegger, Y., Gobet, C., Franken, P., et al. (2018). Clock-dependent chromatin topology modulates circadian transcription and behavior. Genes Dev *32*, 347-358. 10.1101/gad.312397.118.
67. Svensson, V. (2020). Droplet scRNA-seq is not zero-inflated. Nat Biotechnol *38*, 147-150. 10.1038/s41587-019-0379-5.
68. Deng, Q., Ramskold, D., Reinius, B., and Sandberg, R. (2014). Single-cell RNA-seq reveals dynamic, random monoallelic gene expression in mammalian cells. Science *343*, 193-196. 10.1126/science.1245316.
69. Borel, C., Ferreira, P.G., Santoni, F., Delaneau, O., Fort, A., Popadin, K.Y., Garieri, M., Falconnet, E., Ribaux, P., Guipponi, M., et al. (2015). Biased allelic expression in human primary fibroblast single cells. Am J Hum Genet *96*, 70-80. 10.1016/j.ajhg.2014.12.001.
70. Vu, T.N., Wills, Q.F., Kalari, K.R., Niu, N., Wang, L., Rantalainen, M., and Pawitan, Y. (2016). Beta-Poisson model for single-cell RNA-seq data analyses. Bioinformatics *32*, 2128-2135. 10.1093/bioinformatics/btw202.
71. Hildebrandt, F., Andersson, A., Saarenpaa, S., Larsson, L., Van Hul, N., Kanatani, S., Masek, J., Ellis, E., Barragan, A., Mollbrink, A., et al. (2021). Spatial Transcriptomics to define transcriptional patterns of zonation and structural components in the mouse liver. Nat Commun *12*, 7046. 10.1038/s41467-021-27354-w.
72. Ben-Moshe, S., and Itzkovitz, S. (2019). Spatial heterogeneity in the mammalian liver. Nat Rev Gastroenterol Hepatol *16*, 395-410. 10.1038/s41575-019-0134-x.
73. Street, K., Risso, D., Fletcher, R.B., Das, D., Ngai, J., Yosef, N., Purdom, E., and Dudoit, S. (2018). Slingshot: cell lineage and pseudotime inference for single-cell transcriptomics. BMC Genomics *19*, 477. 10.1186/s12864-018-4772-0.
74. Akashi, M., and Takumi, T. (2005). The orphan nuclear receptor RORalpha regulates circadian transcription of the mammalian core-clock Bmal1. Nat Struct Mol Biol *12*, 441-448. 10.1038/nsmb925.
75. Jin, T., and Liu, L. (2008). The Wnt signaling pathway effector TCF7L2 and type 2 diabetes mellitus. Mol Endocrinol *22*, 2383-2392. 10.1210/me.2008-0135.

888 76. Tontonoz, P., Hu, E., Devine, J., Beale, E.G., and Spiegelman, B.M. (1995). PPAR gamma 2 regulates
889 adipose expression of the phosphoenolpyruvate carboxykinase gene. Mol Cell Biol *15*, 351-357.
890 10.1128/MCB.15.1.351.
891 77. Shen, Y., Yue, F., McCleary, D.F., Ye, Z., Edsall, L., Kuan, S., Wagner, U., Dixon, J., Lee, L.,
892 Lobanenkov, V.V., and Ren, B. (2012). A map of the cis-regulatory sequences in the mouse genome.
893 Nature *488*, 116-120. 10.1038/nature11243.
894 78. Lee, T.I., Rinaldi, N.J., Robert, F., Odom, D.T., Bar-Joseph, Z., Gerber, G.K., Hannett, N.M., Harbison,
895 C.T., Thompson, C.M., Simon, I., et al. (2002). Transcriptional regulatory networks in Saccharomyces
896 cerevisiae. Science *298*, 799-804. 10.1126/science.1075090.
897 79. Shen-Orr, S.S., Milo, R., Mangan, S., and Alon, U. (2002). Network motifs in the transcriptional
898 regulation network of Escherichia coli. Nat Genet *31*, 64-68. 10.1038/ng881.
899 80. Takahashi, J.S., Kumar, V., Nakashe, P., Koike, N., Huang, H.C., Green, C.B., and Kim, T.K. (2015).
900 ChIP-seq and RNA-seq methods to study circadian control of transcription in mammals. Methods
901 Enzymol *551*, 285-321. 10.1016/bs.mie.2014.10.059.
902 81. Gekakis, N., Staknis, D., Nguyen, H.B., Davis, F.C., Wilsbacher, L.D., King, D.P., Takahashi, J.S., and
903 Weitz, C.J. (1998). Role of the CLOCK protein in the mammalian circadian mechanism. Science *280*,
904 1564-1569. 10.1126/science.280.5369.1564.
905 82. Takeda, Y., Kang, H.S., Angers, M., and Jetten, A.M. (2011). Retinoic acid-related orphan receptor
906 gamma directly regulates neuronal PAS domain protein 2 transcription in vivo. Nucleic Acids Res *39*,
907 4769-4782. 10.1093/nar/gkq1335.
908 83. Yoshitane, H., Asano, Y., Sagami, A., Sakai, S., Suzuki, Y., Okamura, H., Iwasaki, W., Ozaki, H., and
909 Fukada, Y. (2019). Functional D-box sequences reset the circadian clock and drive mRNA rhythms.
910 Commun Biol *2*, 300. 10.1038/s42003-019-0522-3.
911 84. Chiou, Y.Y., Yang, Y., Rashid, N., Ye, R., Selby, C.P., and Sancar, A. (2016). Mammalian Period
912 represses and de-represses transcription by displacing CLOCK-BMAL1 from promoters in a
913 Cryptochrome-dependent manner. Proc Natl Acad Sci U S A *113*, E6072-E6079.
914 10.1073/pnas.1612917113.
915 85. Koike, N., Yoo, S.H., Huang, H.C., Kumar, V., Lee, C., Kim, T.K., and Takahashi, J.S. (2012).
916 Transcriptional architecture and chromatin landscape of the core circadian clock in mammals. Science
917 *338*, 349-354. 10.1126/science.1226339.
918 86. Furlan-Magaril, M., Ando-Kuri, M., Arzate-Mejia, R.G., Morf, J., Cairns, J., Roman-Figueroa, A.,
919 Tenorio-Hernandez, L., Poot-Hernandez, A.C., Andrews, S., Varnai, C., et al. (2021). The global and
920 promoter-centric 3D genome organization temporally resolved during a circadian cycle. Genome Biol *22*,
921 162. 10.1186/s13059-021-02374-3.
922 87. Greenwell, B.J., Beytebiere, J.R., Lamb, T.M., Bell-Pedersen, D., Merlin, C., and Menet, J.S. (2020).
923 Isoform-specific regulation of rhythmic gene expression by alternative polyadenylation. bioRxiv,
924 2020.2012. 2012.422514.
925 88. Di-Luoffo, M., Daems, C., Bergeron, F., and Tremblay, J.J. (2015). Novel Targets for the Transcription
926 Factors MEF2 in MA-10 Leydig Cells. Biol Reprod *93*, 9. 10.1095/biolreprod.114.127761.
927 89. Xiao, J., Zhou, Y., Lai, H., Lei, S., Chi, L.H., and Mo, X. (2013). Transcription factor NF-Y is a functional
928 regulator of the transcription of core clock gene Bmal1. J Biol Chem *288*, 31930-31936.
929 10.1074/jbc.M113.507038.
930 90. Trott, A.J., and Menet, J.S. (2018). Regulation of circadian clock transcriptional output by
931 CLOCK:BMAL1. PLoS Genet *14*, e1007156. 10.1371/journal.pgen.1007156.
932 91. Skinner, S.O., Xu, H., Nagarkar-Jaiswal, S., Freire, P.R., Zwaka, T.P., and Golding, I. (2016). Single-cell
933 analysis of transcription kinetics across the cell cycle. Elife *5*, e12175. 10.7554/eLife.12175.
934 92. Padovan-Merhar, O., Nair, G.P., Biaesch, A.G., Mayer, A., Scarfone, S., Foley, S.W., Wu, A.R.,
935 Churchman, L.S., Singh, A., and Raj, A. (2015). Single mammalian cells compensate for differences in
936 cellular volume and DNA copy number through independent global transcriptional mechanisms. Mol Cell
937 *58*, 339-352. 10.1016/j.molcel.2015.03.005.

93. Ochiai, H., Sugawara, T., Sakuma, T., and Yamamoto, T. (2014). Stochastic promoter activation affects Nanog expression variability in mouse embryonic stem cells. Sci Rep *4*, 7125. 10.1038/srep07125.
94. Xu, H., Sepulveda, L.A., Figard, L., Sokac, A.M., and Golding, I. (2015). Combining protein and mRNA quantification to decipher transcriptional regulation. Nat Methods *12*, 739-742. 10.1038/nmeth.3446.
95. Fukaya, T., Lim, B., and Levine, M. (2016). Enhancer Control of Transcriptional Bursting. Cell *166*, 358-368. 10.1016/j.cell.2016.05.025.
96. Weideman, A.M.K., Wang, R., Ibrahim, J.G., and Jiang, Y. (2025). Canopy2: tumor phylogeny inference by bulk DNA and single-cell RNA sequencing. Statistics in Biosciences, 1-43.
97. Picelli, S., Faridani, O.R., Bjorklund, A.K., Winberg, G., Sagasser, S., and Sandberg, R. (2014). Full-length RNA-seq from single cells using Smart-seq2. Nat Protoc *9*, 171-181. 10.1038/nprot.2014.006.
98. Hagemann-Jensen, M., Ziegenhain, C., Chen, P., Ramskold, D., Hendriks, G.J., Larsson, A.J.M., Faridani, O.R., and Sandberg, R. (2020). Single-cell RNA counting at allele and isoform resolution using Smart-seq3. Nat Biotechnol *38*, 708-714. 10.1038/s41587-020-0497-0.
99. Dong, M., Thennavan, A., Urrutia, E., Li, Y., Perou, C.M., Zou, F., and Jiang, Y. (2021). SCDC: bulk gene expression deconvolution by multiple single-cell RNA sequencing references. Brief Bioinform *22*, 416-427. 10.1093/bib/bbz166.
100. Stuart, T., Srivastava, A., Madad, S., Lareau, C.A., and Satija, R. (2021). Single-cell chromatin state analysis with Signac. Nat Methods *18*, 1333-1341. 10.1038/s41592-021-01282-5.
101. Zhu, J., Li, C., Gong, C., and Li, X. (2018). Regulation of Pol II Pausing Is Involved in Daily Gene Transcription in the Mouse Liver. J Biol Rhythms *33*, 350-362. 10.1177/0748730418779526.
102. Le Martelot, G., Canella, D., Symul, L., Migliavacca, E., Gilardi, F., Liechti, R., Martin, O., Harshman, K., Delorenzi, M., Desvergne, B., et al. (2012). Genome-wide RNA polymerase II profiles and RNA accumulation reveal kinetics of transcription and associated epigenetic changes during diurnal cycles. PLoS Biol *10*, e1001442. 10.1371/journal.pbio.1001442.
103. Atger, F., Gobet, C., Marquis, J., Martin, E., Wang, J., Weger, B., Lefebvre, G., Descombes, P., Naef, F., and Gachon, F. (2015). Circadian and feeding rhythms differentially affect rhythmic mRNA transcription and translation in mouse liver. Proc Natl Acad Sci U S A *112*, E6579-6588. 10.1073/pnas.1515308112.
104. Satpathy, A.T., Granja, J.M., Yost, K.E., Qi, Y., Meschi, F., McDermott, G.P., Olsen, B.N., Mumbach, M.R., Pierce, S.E., Corces, M.R., et al. (2019). Massively parallel single-cell chromatin landscapes of human immune cell development and intratumoral T cell exhaustion. Nat Biotechnol *37*, 925-936. 10.1038/s41587-019-0206-z.
105. Germain, P.L., Lun, A., Garcia Meixide, C., Macnair, W., and Robinson, M.D. (2021). Doublet identification in single-cell sequencing data using scDblFinder. F1000Res *10*, 979. 10.12688/f1000research.73600.2.
106. Xu, S., Hu, E., Cai, Y., Xie, Z., Luo, X., Zhan, L., Tang, W., Wang, Q., Liu, B., Wang, R., et al. (2024). Using clusterProfiler to characterize multiomics data. Nat Protoc *19*, 3292-3320. 10.1038/s41596-024-01020-z.
107. Zheng, G.X., Terry, J.M., Belgrader, P., Ryvkin, P., Bent, Z.W., Wilson, R., Ziraldo, S.B., Wheeler, T.D., McDermott, G.P., Zhu, J., et al. (2017). Massively parallel digital transcriptional profiling of single cells. Nat Commun *8*, 14049. 10.1038/ncomms14049.
108. Haghverdi, L., Lun, A.T.L., Morgan, M.D., and Marioni, J.C. (2018). Batch effects in single-cell RNA-sequencing data are corrected by matching mutual nearest neighbors. Nat Biotechnol *36*, 421-427. 10.1038/nbt.4091.
109. Baran, Y., Bercovich, A., Sebe-Pedros, A., Lubling, Y., Giladi, A., Chomsky, E., Meir, Z., Hoichman, M., Lifshitz, A., and Tanay, A. (2019). MetaCell: analysis of single-cell RNA-seq data using K-nn graph partitions. Genome Biol *20*, 206. 10.1186/s13059-019-1812-2.
110. Ding, H., Meng, L., Liu, A.C., Gumz, M.L., Bryant, A.J., McClung, C.A., Tseng, G.C., Esser, K.A., and Huo, Z. (2021). Likelihood-based tests for detecting circadian rhythmicity and differential circadian patterns in transcriptomic applications. Brief Bioinform *22*. 10.1093/bib/bbab224.
111. Parker, T. (2017). Finite-sample distributions of the Wald, likelihood ratio, and Lagrange multiplier test statistics in the classical linear model. Communications in Statistics-Theory and Methods *46*, 5195-5202.

Figure 1

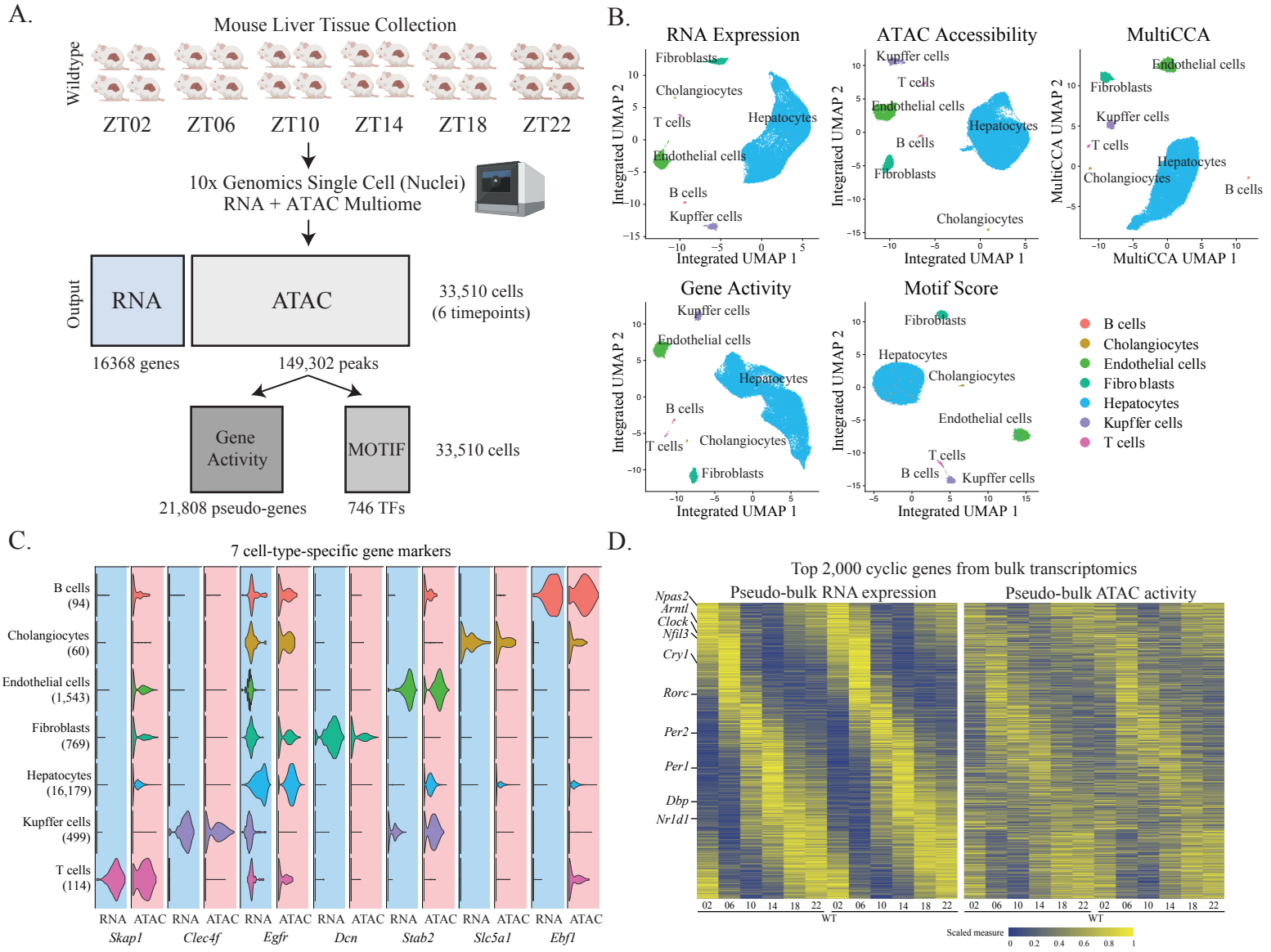
A.
Mouse Liver Tissue Collection
Wildtype
ZT02
ZT06
ZT10
ZT14
ZT18
ZT22
10x Genomics Single Cell (Nuclei)
RNA + ATAC Multiome
Output
RNA
ATAC
33,510 cells
(6 timepoints)
16368 genes
149,302 peaks
Gene Activity
MOTIF
33,510 cells
21,808 pseudo-genes
746 TFs
B.
RNA Expression
ATAC Accessibility
MultiCCA
Gene Activity
Motif Score
Integrated UMAP 1
Integrated UMAP 2
MultiCCA UMAP 1
MultiCCA UMAP 2
Fibroblasts
Cholangiocytes
T cells
Endothelial cells
Hepatocytes
B cells
Kupffer cells
C.
7 cell-type-specific gene markers
B cells (94)
Cholangiocytes (60)
Endothelial cells (1,543)
Fibroblasts (769)
Hepatocytes (16,179)
Kupffer cells (499)
T cells (114)
RNA
ATAC
Skap1
Clec4f
Egfr
Dcn
Stab2
Slc5a1
Ebf1
D.
Top 2,000 cyclic genes from bulk transcriptomics
Pseudo-bulk RNA expression
Pseudo-bulk ATAC activity
Npas2
Arntl
Clock
Nfil3
Cry1
Rorc
Per2
Per1
Dbp
Nr1d1
02
06
10
14
18
22
WT
Scaled measure
0
0.2
0.4
0.6
0.8
1

Figure 2

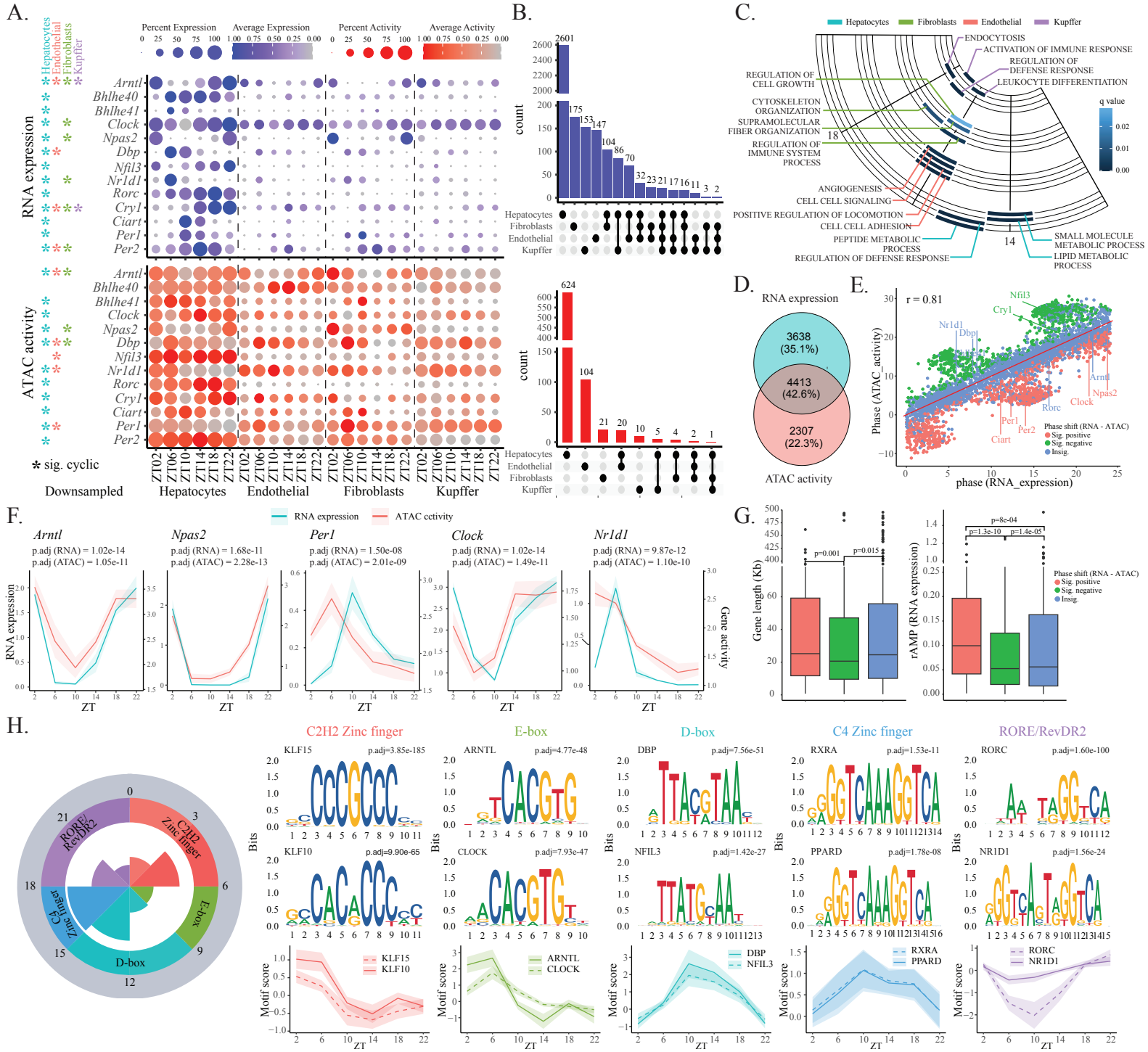
A.
Percent Expression
Average Expression
Percent Activity
Average Activity
Hepatocytes
Endothelial
Fibroblasts
Kupffer
RNA expression
ATAC activity
Arntl
Bhlhe40
Bhlhe41
Clock
Npas2
Dbp
Nfil3
Nr1d1
Rorc
Cry1
Ciart
Per1
Per2
* sig. cyclic
Downsampled
ZT02 ZT06 ZT10 ZT14 ZT18 ZT22
B.
count
C.
ENDOCYTOSIS
ACTIVATION OF IMMUNE RESPONSE
REGULATION OF DEFENSE RESPONSE
LEUKOCYTE DIFFERENTIATION
REGULATION OF CELL GROWTH
CYTOSKELETON ORGANIZATION
SUPRAMOLECULAR FIBER ORGANIZATION
REGULATION OF IMMUNE SYSTEM PROCESS
ANGIOGENESIS
CELL CELL SIGNALING
POSITIVE REGULATION OF LOCOMOTION
CELL CELL ADHESION
PEPTIDE METABOLIC PROCESS
REGULATION OF DEFENSE RESPONSE
SMALL MOLECULE METABOLIC PROCESS
LIPID METABOLIC PROCESS
q value
D.
RNA expression
3638 (35.1%)
4413 (42.6%)
2307 (22.3%)
ATAC activity
E.
r = 0.81
Phase (ATAC_activity)
phase (RNA_expression)
Phase shift (RNA - ATAC)
Sig. positive
Sig. negative
Insig.
F.
RNA expression
ATAC ectivity
Arntl
p.adj (RNA) = 1.02e-14
p.adj (ATAC) = 1.05e-11
Npas2
p.adj (RNA) = 1.68e-11
p.adj (ATAC) = 2.28e-13
Per1
p.adj (RNA) = 1.50e-08
p.adj (ATAC) = 2.01e-09
Clock
p.adj (RNA) = 1.02e-14
p.adj (ATAC) = 1.49e-11
Nr1d1
p.adj (RNA) = 9.87e-12
p.adj (ATAC) = 1.10e-10
Gene activity
ZT
G.
Gene length (Kb)
rAMP (RNA expression)
p=0.001
p=0.015
p=8e-04
p=1.3e-10
p=1.4e-05
H.
C2H2 Zinc finger
E-box
D-box
C4 Zinc finger
RORE/RevDR2
KLF15
p.adj=3.85e-185
ARNTL
p.adj=4.77e-48
DBP
p.adj=7.56e-51
RXRA
p.adj=1.53e-11
RORC
p.adj=1.60e-100
KLF10
p.adj=9.90e-65
CLOCK
p.adj=7.93e-47
NFIL3
p.adj=1.42e-27
PPARD
p.adj=1.78e-08
NR1D1
p.adj=1.56e-24
Bits
Motif score

Figure 3

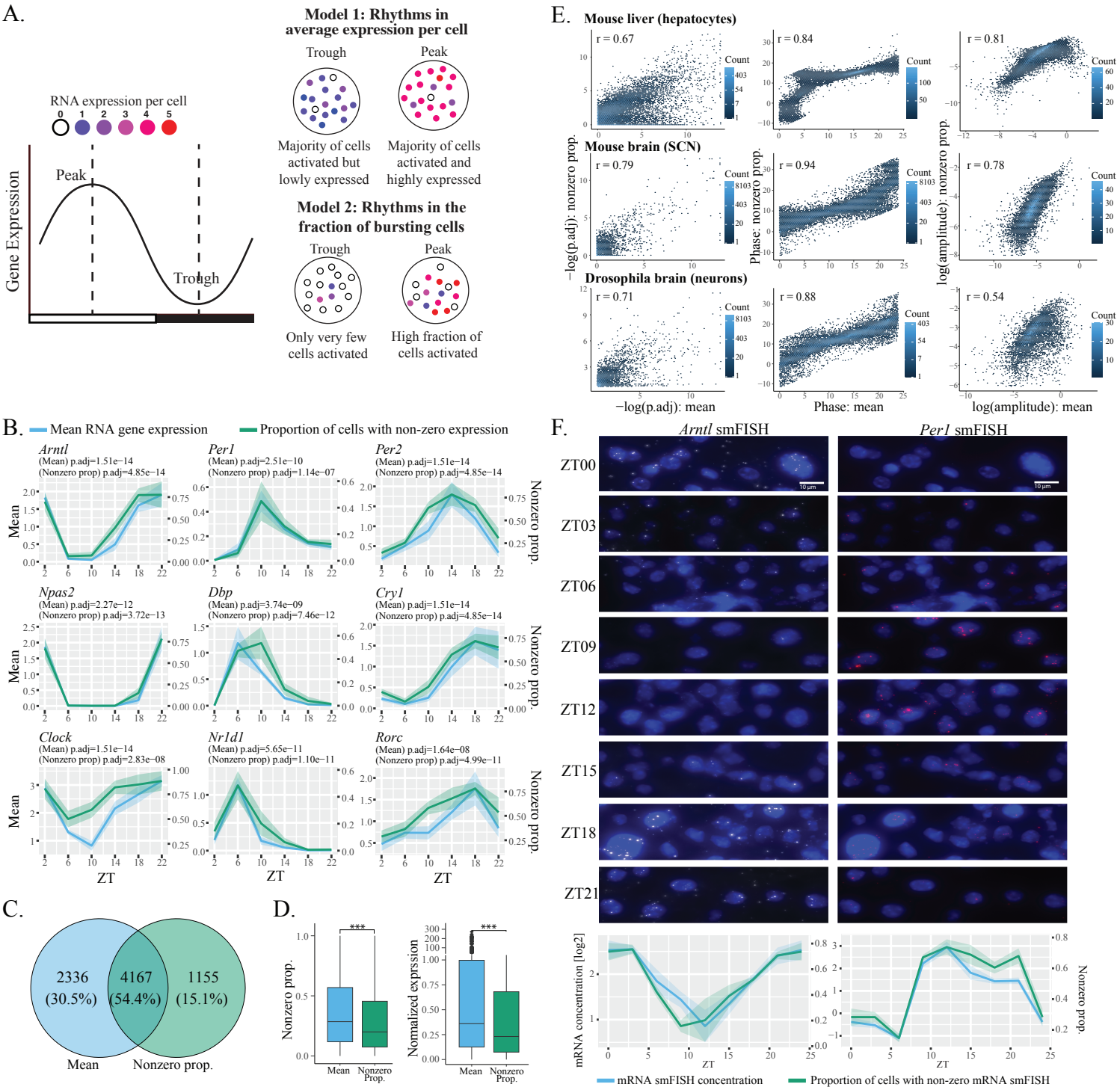
A.
RNA expression per cell
0 1 2 3 4 5
Gene Expression
Peak
Trough
Model 1: Rhythms in average expression per cell
Trough
Peak
Majority of cells activated but lowly expressed
Majority of cells activated and highly expressed
Model 2: Rhythms in the fraction of bursting cells
Trough
Peak
Only very few cells activated
High fraction of cells activated
B.
Mean RNA gene expression
Proportion of cells with non-zero expression
Arntl
(Mean) p.adj=1.51e−14
(Nonzero prop) p.adj=4.85e−14
Per1
(Mean) p.adj=2.51e−10
(Nonzero prop) p.adj=1.14e−07
Per2
(Mean) p.adj=1.51e−14
(Nonzero prop) p.adj=4.85e−14
Npas2
(Mean) p.adj=2.27e−12
(Nonzero prop) p.adj=3.72e−13
Dbp
(Mean) p.adj=3.74e−09
(Nonzero prop) p.adj=7.46e−12
Cry1
(Mean) p.adj=1.51e−14
(Nonzero prop) p.adj=4.85e−14
Clock
(Mean) p.adj=1.51e−14
(Nonzero prop) p.adj=2.83e−08
Nr1d1
(Mean) p.adj=5.65e−11
(Nonzero prop) p.adj=1.10e−11
Rorc
(Mean) p.adj=1.64e−08
(Nonzero prop) p.adj=4.99e−11
Mean
Nonzero prop.
ZT
C.
2336 (30.5%)
4167 (54.4%)
1155 (15.1%)
Mean
Nonzero prop.
D.
Nonzero prop.
Normalized exprssion
Mean
Nonzero Prop.
E.
Mouse liver (hepatocytes)
r = 0.67
r = 0.84
r = 0.81
Mouse brain (SCN)
r = 0.79
r = 0.94
r = 0.78
Drosophila brain (neurons)
r = 0.71
r = 0.88
r = 0.54
Count
−log(p.adj): nonzero prop.
Phase: nonzero prop.
log(amplitude): nonzero prop.
−log(p.adj): mean
Phase: mean
log(amplitude): mean
F.
Arntl smFISH
Per1 smFISH
ZT00
ZT03
ZT06
ZT09
ZT12
ZT15
ZT18
ZT21
10 µm
mRNA concentration [log2]
Nonzero prop.
ZT
mRNA smFISH concentration
Proportion of cells with non-zero mRNA smFISH

Figure 4

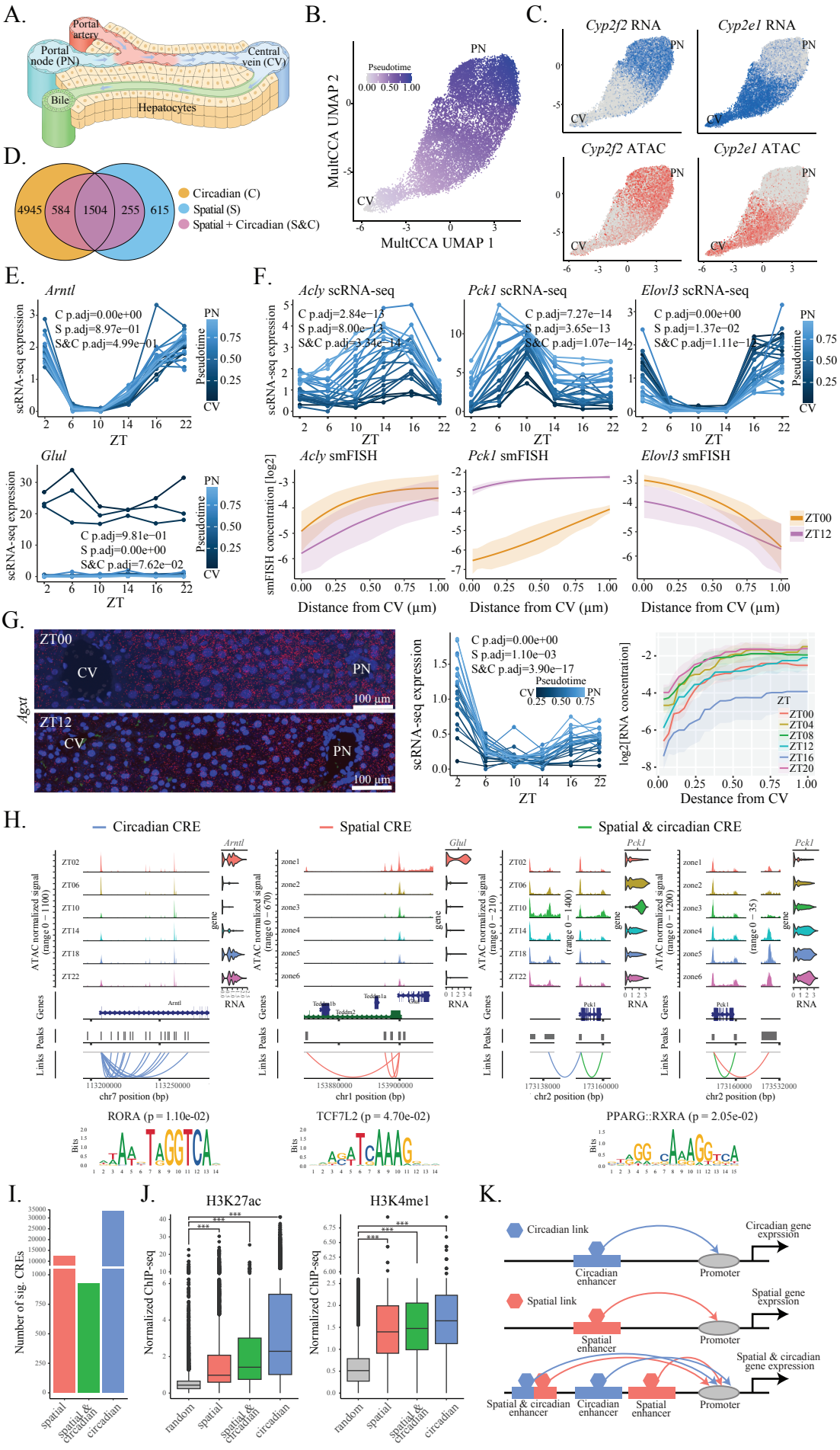
A.
Portal artery
Portal node (PN)
Central vein (CV)
Bile
Hepatocytes
B.
Pseudotime
0.00 0.50 1.00
PN
CV
MultCCA UMAP 2
MultCCA UMAP 1
C.
Cyp2f2 RNA
Cyp2e1 RNA
Cyp2f2 ATAC
Cyp2e1 ATAC
D.
4945
584
1504
255
615
Circadian (C)
Spatial (S)
Spatial + Circadian (S&C)
E.
Arntl
C p.adj=0.00e+00
S p.adj=8.97e−01
S&C p.adj=4.99e−01
Glul
C p.adj=9.81e−01
S p.adj=0.00e+00
S&C p.adj=7.62e−02
scRNA-seq expression
ZT
Pseudotime
F.
Acly scRNA-seq
C p.adj=2.84e−13
S p.adj=8.00e−13
S&C p.adj=3.34e−14
Pck1 scRNA-seq
C p.adj=7.27e−14
S p.adj=3.65e−13
S&C p.adj=1.07e−14
Elovl3 scRNA-seq
C p.adj=0.00e+00
S p.adj=1.37e−02
S&C p.adj=1.11e−12
Acly smFISH
Pck1 smFISH
Elovl3 smFISH
smFISH concentration [log2]
Distance from CV (μm)
ZT00
ZT12
G.
ZT00
ZT12
CV
PN
Agxt
100 μm
C p.adj=0.00e+00
S p.adj=1.10e−03
S&C p.adj=3.90e−17
log2[RNA concentration]
Destance from CV
ZT00
ZT04
ZT08
ZT12
ZT16
ZT20
H.
Circadian CRE
Spatial CRE
Spatial & circadian CRE
ATAC normalized signal
Genes
Peaks
Links
RNA
chr7 position (bp)
chr1 position (bp)
chr2 position (bp)
RORA (p = 1.10e-02)
TCF7L2 (p = 4.70e-02)
PPARG::RXRA (p = 2.05e-02)
I.
Number of sig. CREs
spatial
spatial & circadian
circadian
J.
H3K27ac
H3K4me1
Normalized ChIP-seq
random
spatial
spatial & circadian
circadian
K.
Circadian link
Circadian gene exprssion
Circadian enhancer
Promoter
Spatial link
Spatial gene exprssion
Spatial enhancer
Spatial & circadian gene expression
Spatial & circadian enhancer
Circadian enhancer
Spatial enhancer
Promoter

Figure 5

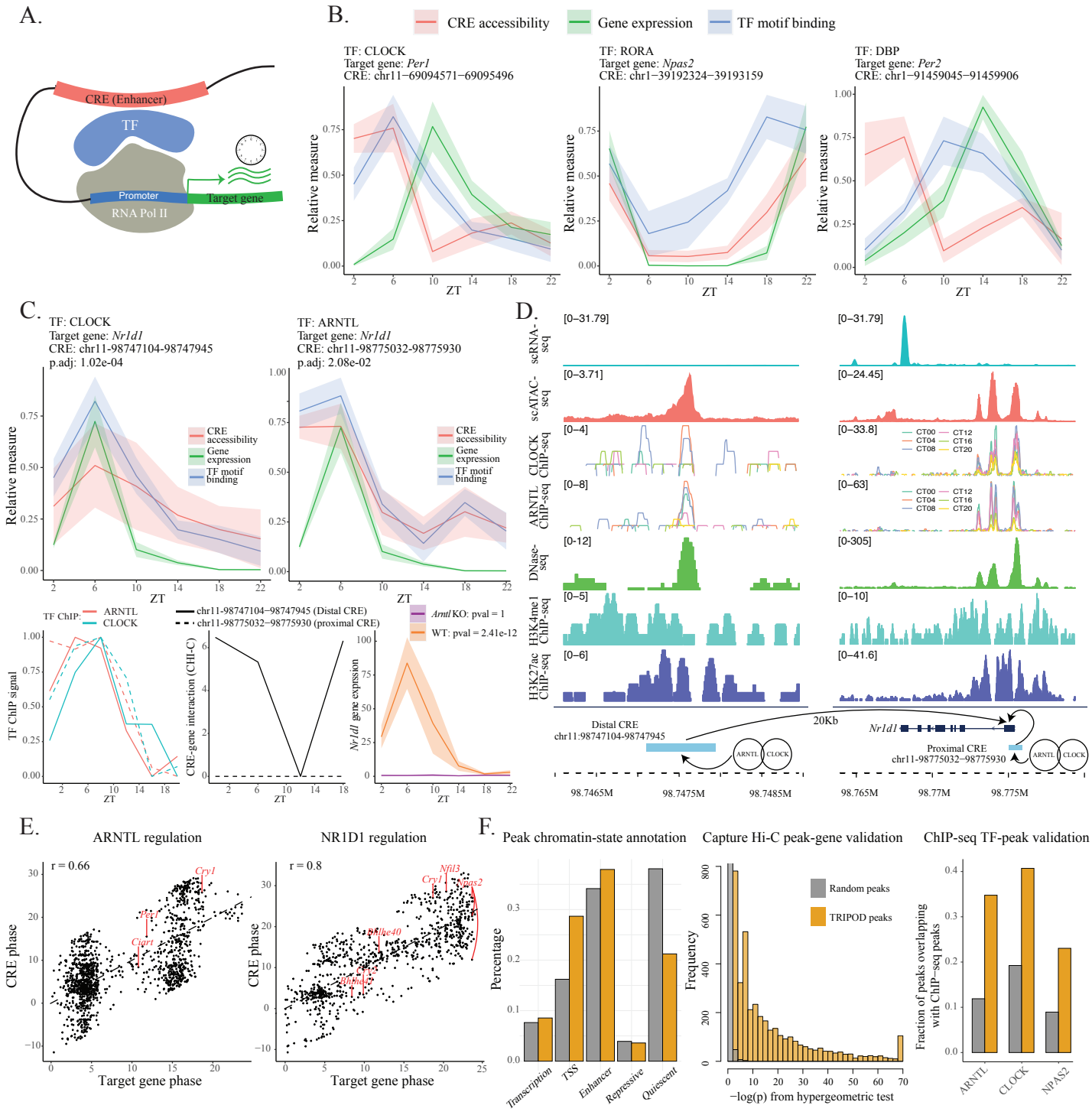

A.
CRE (Enhancer)
TF
Promoter
RNA Pol II
Target gene
B.
CRE accessibility
Gene expression
TF motif binding
TF: CLOCK
Target gene: Per1
CRE: chr11−69094571−69095496
TF: RORA
Target gene: Npas2
CRE: chr1−39192324−39193159
TF: DBP
Target gene: Per2
CRE: chr1−91459045−91459906
Relative measure
ZT
C.
TF: CLOCK
Target gene: Nr1d1
CRE: chr11-98747104-98747945
p.adj: 1.02e-04
TF: ARNTL
Target gene: Nr1d1
CRE: chr11-98775032-98775930
p.adj: 2.08e-02
TF ChIP: ARNTL CLOCK
chr11-98747104−98747945 (Distal CRE)
chr11-98775032−98775930 (proximal CRE)
Arntl KO: pval = 1
WT: pval = 2.41e-12
TF ChIP signal
CRE-gene interaction (CHI-C)
Nr1d1 gene expression
D.
scRNA-seq
scATAC-seq
CLOCK ChIP-seq
ARNTL ChIP-seq
DNase-seq
H3K4me1 ChIP-seq
H3K27ac ChIP-seq
Distal CRE
chr11:98747104-98747945
Proximal CRE
chr11-98775032−98775930
20Kb
Nr1d1
98.7465M
98.7475M
98.7485M
98.765M
98.77M
98.775M
E.
ARNTL regulation
NR1D1 regulation
r = 0.66
r = 0.8
CRE phase
Target gene phase
Cry1
Per1
Ciart
Nfil3
Npas2
Bhlhe40
F.
Peak chromatin-state annotation
Capture Hi-C peak-gene validation
ChIP-seq TF-peak validation
Percentage
Transcription
TSS
Enhancer
Repressive
Quiescent
Frequency
Random peaks
TRIPOD peaks
−log(p) from hypergeometric test
Fraction of peaks overlapping with ChIP−seq peaks
ARNTL
CLOCK
NPAS2